Surface & Coatings Technology 521 (2026) 133101

Contents lists available at ScienceDirect

Surface & Coatings Technology

journal homepage: www.elsevier.com/locate/surfcoat

Plasma electrolytic oxidation of aluminium using conventional anodizing precursors and electrolytic colouring with Cu, Sn and Ni

I. Hidalgo-González [*], E. Matykina, R. Arrabal

Departamento de Ingeniería Química y de Materiales, Facultad de Ciencias Químicas, Universidad Complutense de Madrid, 28040, Madrid, Spain

ARTICLE INFO

Keywords:
Aluminium
Plasma electrolytic oxidation
Anodizing
Electrolytic colouring
Copper
Tin
Nickel
Soft sparking
Wear
Corrosion

ABSTRACT

Previous studies have demonstrated that conventional anodizing precursors can reduce the energy consumption of plasma electrolytic oxidation (PEO) by facilitating the transition to the soft sparking regime, which produces denser coatings with improved wear performance. Here, we investigate the influence of anodizing precursors electrolytically coloured with Cu, Sn and Ni prior to PEO. Metal species accelerate the transition to soft sparking, with Cu exhibiting the greatest energy savings (~ 54 %) due to deposits in the inner precursor regions promoting dielectric breakdown. Wear resistance of the most energy-efficient system (A(Cu)-PEO) was comparable to Cu-free coatings (PEO, A-PEO), although A-PEO exhibited a lower friction coefficient (~ 0.69) after long sliding distances, linked to a more compact coating from extended soft sparking. Electrochemical impedance spectroscopy (EIS) revealed that Cu led to a weaker barrier layer in A(Cu)-PEO, yet the substrate showed negligible corrosion after 28 days in 3.5 wt% NaCl. Overall, A-PEO and A(Cu)-PEO are viable alternatives to conventional PEO, offering substantial energy savings without compromising performance.

1. Introduction

PEO is an environmentally friendly surface treatment applied on Al alloys in alkaline electrolytes for high added-value applications under demanding service conditions. High voltages during PEO (~ 300–400 V) induce the dielectric breakdown of the oxide film and the accompanying gas, which is evidenced in the form of short-lived microdischarges throughout the oxide layer growth [1–3]. The ceramic coatings produced as a result can reach thicknesses in the hundreds of micrometers, and are characterized by excellent corrosion and wear resistance, high hardness, elevated thermal stability and exceptional adhesion to the substrate [3–6]. Three distinct zones can be identified within the PEO coating: (I) an outer porous layer constituting approximately 5–30 % of the coating thickness, (II) a dense intermediate layer characterized by microcracks and submicrometer-sized pores, and (III) a barrier layer approximately 300 nm-thick in contact with the substrate [7]. Despite the significant advantages offered by PEO, its high energy costs (20–50 times higher than those of conventional anodizing) and low yields (averaging around 25 % current efficiency) limit its industrial application to specific sectors, such as aerospace and oil and gas.

In order to reduce energy consumption, several strategies have been successfully developed in recent years, mainly for aluminium and magnesium alloys. The most notable approaches include: (I) cell geometry design [8,9]; (II) modification of electrical parameters (e.g. frequency, current density, or current mode) [10–12]; (III) electrolyte design by using additives, such as complexing agents [13,14], or by incorporating particles to produce composite coatings [15]; (IV) flash-PEO or short treatments [16,17]; (V) sequential treatments based on two-step PEO [18] and the use of precursors such as conversion coatings [19] and conventional anodic films [16–19]. It should be noted that often PEO coating studies forgo the explicit quantification of the energy savings. Some exceptions are the studies by Yerokhin et al. [20], Xie et al. [21], Tian et al. [22], Cheng et al., Li et al. [23] and our own previous studies on conventional anodic film precursors. In the latter, the reported energy savings ranged from 40 % to 70 %, depending on the Al alloy, the morphology and thickness of the precursor film and the addition of suspended particles in the electrolyte [15,24].

The presence of an oxide layer, formed by traditional anodizing in an acidic electrolyte (e.g., sulfuric, phosphoric or oxalic), promotes the early establishment of the soft sparking regime during PEO of aluminium alloys. Note that most of the works on energy savings do not deal with this regime, with the exception of those using anodic film precursors. The soft sparking regime is characterized by an increased growth rate and the formation of the dense intermediate layer, which is

---

* Corresponding author.
E-mail address: ihidal01@ucm.es (I. Hidalgo-González).

https://doi.org/10.1016/j.surfcoat.2025.133101
Received 7 October 2025; Received in revised form 16 December 2025; Accepted 19 December 2025

responsible for the excellent mechanical and wear properties of the coating [25,26]. The soft sparking regime begins once the coating reaches a critical thickness, leading to microdischarges that emit less noise and spread more uniformly across the entire surface, resulting in formation of a dense intermediate layer of the PEO coatings. The transition is favoured when the cathodic current density (J_c) exceeds the anodic one (J_a), resulting in a current ratio $\left(R = \frac{J_c}{J_a}\right)$ greater than 1 [27].

Additional factors that influence the nature of discharges and the transition to soft sparking include frequency and current density, as well as the composition and microstructure of the substrate. For instance, secondary phases rich in elements such as Fe and Cu have a strong effect on the location and intensity of the discharges [28], while high frequency and current density as well as fine microstructures in additively manufactured alloys promote soft sparking [10,29].

Metal precursors applied via thermal spraying or magnetron sputtering have been used in the past to form PEO coatings on non-anodizable substrates [30] or probe the mechanism of PEO coating growth [31]. However, to the best of our knowledge, the anodic films and metal deposit combination has not been used as a strategy for energy savings in PEO. This approach is enabled through electrodeposition, which is a simple and well-established method in anodizing facilities for producing a wide range of colours.

The present work proposes a new precursor system based on the combination of conventional anodizing followed by electrolytic colouring. This approach is based on the hypothesis that metallic deposits may modify the local properties of the precursor material and facilitate dielectric breakdown and the transition to the soft sparking regime. Three different precursor systems were developed depending on the deposited metal (Sn, Cu, or Ni). The PEO process was subsequently applied to the different precursor coatings. The specimens were characterized using several techniques, including scanning electron microscopy (SEM), X-ray diffraction (XRD), optical profilometry, as well as Vickers microhardness and colour measurements. In addition, the influence of the different precursor systems on the coating growth and soft sparking transition was studied. Wear resistance of the selected precursor-based and precursor-free PEO systems was examined using ball-on-flat wear tests. Corrosion resistance of the specimens was evaluated using electrochemical impedance spectroscopy (EIS) during 28 days-long immersion tests in 3.5 wt% NaCl.

2. Materials and methods

2.1. Surface preparation

The base material used in this work was the Al-1085 alloy (30 × 20 × 1 mm). All specimens were subjected to the following commercial surface pretreatment to ensure proper surface activation prior to the precursors and PEO treatments and to align with the standard surface preparation procedures employed in anodizing plants: (I) alkaline cleaning in a 50 g/L BONDERITE C-AK 4215 NC solution for 10 min at 60 °*C*. This contains $Na_2B_4O_7{\cdot}12H_2O$, fluorosilicates, and organic surfactants that remove oils, organic contaminants and other residues. (II) Alkaline etching in a 38 g/L BONDERITE C-AK ALUM ETCH 2 AERO solution for 2 min at 40 °*C*. This is composed of NaOH and Na_3PO_4 that dissolve the native oxide film, produce a controlled micro-roughened surface and remove surface segregations and plastically deformed layers. (III) Immersion in a 20 % acid (HNO_3 and HF mixture) aqueous solution of BONDERITE C-IC SMUTGO NC AERO for 5 min at room temperature. This step removes insoluble intermetallic particles (i.e. "smut") that otherwise would modify the anodizing and PEO processes. After surface pretreatment, the specimens were rinsed with deionized water and dried with warm air. The electric contact was established through a copper wire, the working area (3 cm^2) was defined using an epoxy resin (Red Stopping off Lacquer, MacDermid Enthone).

2.2. Anodizing, electrolytic colouring and PEO treatments

The electrical parameters and electrolyte baths employed for the treatments are summarized in Table 1. A 20 μm-thick precursor layer was formed by anodizing using a DC power supply (SM400-AR-8, Delta Elektronika). The process was conducted in a 1 L double-walled glass cell under continuous stirring at ~300 rpm and connected to a closed-loop cooling system (Huber mini-chiller Plus, with Huber SynOil, M10.120.08 fluid). A cylindrical plate made of pure aluminium (∅ ~ 10 cm) was used as the counter electrode. Electrolytic colouring was carried out in the same setup as the anodizing process, using an AC power supply (EAC-S2000, ET Systems Electronic). A KUSB-3116 Keithley data acquisition card was employed to record the root mean square (RMS) voltage and current responses throughout the treatment. A 2-channel Tektronix TDS 2012B oscilloscope with a 100 MHz sampling rate was used to monitor and record the instantaneous voltage and current waveforms. Several colouring methods were performed depending on the deposited metal: tin, copper, or nickel. To determine the amount of metal deposited, larger specimens (50 cm^2) were used and weighed before and after the electrolytic colouring process, following a drying step (RADWAG, AS220.R2-Plus, readability 0.1 mg). The deposited mass was then converted to mmol cm^{-2} by accounting for the atomic weights of Cu, Sn and Ni. All measurements were performed in triplicate.

PEO coatings were carried out using the previously described AC power supply. The process was performed in a 2 L double-walled glass cell connected to a closed-loop cooling system (WK 120 LAUDA) and maintained under continuous stirring at 300 rpm, in conditions similar to those used for the other treatments. A cylindrical mesh made of AISI 316 L stainless steel (∅ ~ 15 cm) was used as the counter electrode.

The energy consumption values ($kW{\cdot}h{\cdot}m^{-2}$) for anodizing, electrolytic colouring and PEO (E_A, E_C and E_{PEO}) were calculated by integrating their respective current-time and voltage-time curves (Eq. (1)). For electrolytic colouring and PEO, the reported values correspond to apparent energy consumption, as RMS current and voltages signals were used.

$$E_{treatment} = \int_{t_0}^{t} Vi\, dt \tag{1}$$

where ($E_{treatment}$) refers to E_A, E_C or E_{PEO}; (V) is the voltage; (i) is the current density; and (t) is the time of the process. The total specific energy consumption (E_{TOTAL}, $kW{\cdot}h{\cdot}m^{-2}{\cdot}\mu m^{-1}$) was calculated by summing the energy consumption of the applied treatments and dividing by the final thickness of the resultant coating.

2.3. Gas evolution measurements

Gas evolution during the electrolytic colouring and PEO processes was evaluated using an analytical balance (RADWAG, AS220.R2-Plus). A schematic diagram of the experimental setup and testing procedure is shown in Fig. 1. The sample was suspended from the balance and completely enclosed by a larger glass cylinder, which served as a gas collector. Gas bubbles are gradually released from the surface of the sample and accumulate at the top of the glass cylinder (Fig. 1(a)). The continuous accumulation of gas generates an upward buoyant force, which results in a detectable change in the weight recorded by the balance. The gas volume generated was calculated using the measured mass variation over time and the known electrolyte density (electrolytic colouring baths ~1.03 g/mL, PEO bath ~1 g/mL) as described in [32]. The mass increase was recorded at 5 s intervals until the end of the process. The conditions used for gas evolution measurement during the electrolytic colouring and PEO process were in accordance with those previously described. In neither case was agitation applied during the treatment to collect the evolved gas better.

Table 1
Treatment conditions for anodizing, electrolytic colouring and PEO at 25 °C.

Anodizing	
Electrolytic bath	15 wt% of H_2SO_4
Current density (mA·cm^{-2})	50
Time (s)	800 (with 200 s of initial ramp)
Electrolytic colouring	
Electrolytic baths	Sn colouring: 15 g/L $SnSO_4$, 27 g/L H_2SO_4, 2 g/L $C_7H_6O_6S{\cdot}2H_2O$ (pH: 0.9; σ: 115 mS/cm) Cu colouring: 20 g/L $CuSO_4$, 6 g/L H_2SO_4 (pH: 1.6; σ: 62 mS/cm) Ni colouring: 30 g/L $NiSO_4$, 30 g/L H_3BO_3 (pH: 4.6; σ: 9.3 mS/cm)
RMS voltage (V)	15
Frequency (Hz)	50
Time (s)	600 (with 60 s of initial and final ramps)
Waveform	Sinusoidal
PEO	
Electrolytic bath	2.8 g/L KOH, 5 g/L $Na_3PO_4{\cdot}12H_2O$, 10.5 g/L NaO $(SiO_2)_x{\cdot}xH_2O$ (specific weight 1.39 g/L) (pH: 12.5; σ: 13.6 mS/cm)
Current density (mA·cm^{-2})	500
Voltage (V)	+490/−110
Frequency (Hz)	50
Time (s)	600 s after current drop[a] (60 s initial and final ramps)
Waveform	Square

[a] The current drop refers to the moment when the RMS current density decreases below the limit value of 500 mA·cm^{-2} ($i < 500$ mA·cm^{-2}). This time point is characteristic of each PEO system and coincides with the moment when the set RMS voltage is reached.

2.4. Coating characterization methods

The morphology and elemental composition of the specimens were characterized by scanning electron microscopy (SEM). JEOL JSM-6400 and JEOL JSM-IT700HR electron microscopes were employed. Coating thickness was measured using the eddy current method (ISOSCOPE FMP10, Fischer). A total of 10 measurements were performed per specimen. Subsequently, the results were confirmed through SEM image characterization. All cross-sectional observations were performed on specimens that were cut, embedded in epoxy resin (NXmet, XH40, XF40) and polished up to 1 μm diamond paste. For selected specimens, cross sections were prepared by fracture after 1 min immersion in liquid nitrogen, as noted in the text where relevant. X-ray diffraction analysis (XRD) was carried out by a Philips X'Pert-MPD diffractometer (Cu $K_\alpha = 1.540598$ Å) for a scan range of 2θ from 10° to 90°, with a scanning speed of 0.04°/s (2 s/step) and an incidence angle of 90°. A focus variation optical profilometer with a × 50 lens (Alicona, InfiniteFocusSL) was used to study surface roughness. Two roughness parameters were analysed: S_a (average height of the selected area) and S_{10z} (sum of the average height of the five highest peaks and the average depth of the five deepest valleys). The colour of the coatings was evaluated using the CIELAB colour space. Three colour parameters were studied on each sample: L* (lightness), a* (+a* for red colours/−a* for green colours) and b* (+b* for yellow colours/−b* for blue colours). The analysis was carried out with a UV–Vis Shimadzu 2600i spectrophotometer (integrating sphere: ISR-2600) in wavelength range from 380 to 780 nm. The hardness of the specimens was evaluated using an AKASHI MVK-E3 microhardness tester with a 0.025 kg load. Average hardness values correspond to five measurements.

2.5. Wear and corrosion tests

The wear tests were carried out using a MT 60/NI tribometer (Microtest) in the ball-on-flat mode. The applied normal force was 10 N and the sliding speed was 50 mm/s (equivalent to 2.5 rev/s), for a total sliding distance of 600 m. The sample acted as the sliding plate, and the WC ball (diameter ~ 6 mm and grade G10) served as the counterpart. For each surface treatment, wear tests were performed in three different regions on the same sample under room temperature (T ~ 25 °C) and dry conditions. The wear tracks were characterized using the optical profilometer previously described, with a × 10 lens. An average wear track profile with a width of 5 mm was obtained for each specimen using the IF-Measure Suite 5.3 software. The wear volume (mm^3) was calculated as the cumulative integral of the wear track profile multiplied by its length (10 mm). Based on this value, the wear rate (mm^3·N^{-1}·m^{-1}) was

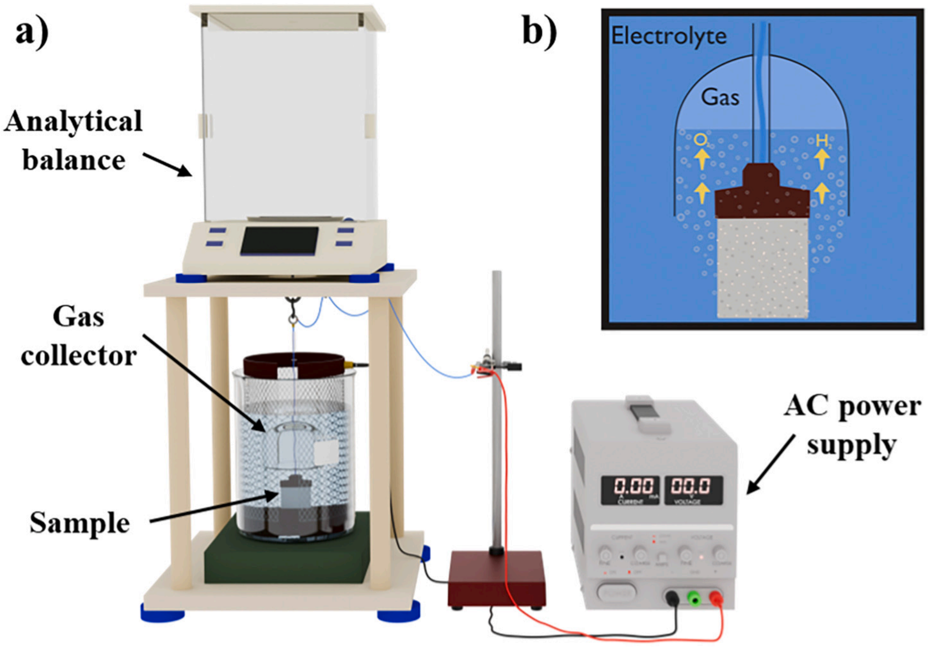

Fig. 1. Schematic representation of the apparatus (a) and the experimental procedure (b) employed to measure gas evolution in the electrolytic colouring and PEO treatment.

also determined according to Eq. (2).

$$\text{Wear rate } (\mathrm{W_r}) = \frac{\text{Wear volume } (\mathrm{mm}^3)}{\text{Load (N)}\cdot\text{Sliding distance (m)}} \tag{2}$$

EIS technique was employed to evaluate the corrosion resistance of the specimens over 28 days in a 3.5 wt% NaCl aqueous solution. The measurements were recorded using a GillAC potentiostat (ACM Instruments) connected to a three-electrode electrochemical cell: a reference electrode Ag/AgCl (3 M KCl), a graphite counter electrode, and a working electrode or sample (~ 1 cm^2 exposed area). The measurements were recorded over a frequency range from 100 kHz to 0.01 Hz, with a sinusoidal perturbation amplitude of 10 mV. The samples subjected to wear and corrosion tests were subsequently characterized by SEM in order to investigate the mechanisms involved.

3. Results and discussion

3.1. Voltage-current responses during anodizing and electrolytic colouring

Fig. 2 presents the typical voltage-current response of the pre-anodizing treatment controlled by constant current conditions which includes an initial 200 s ramp. The process is carried out until the formation of a porous oxide layer of 20 μm is achieved, which is the optimal thickness as reported in previous studies [24,25]. The graph shows a progressive increase in voltage throughout the first few seconds of the treatment, in accordance with the current slope. During this stage, the growth and thickening of the barrier layer takes place. Then, the current reaches the set value and the voltage remains relatively constant at approximately 20 V, leading to the uniform growth of the porous layer [33].

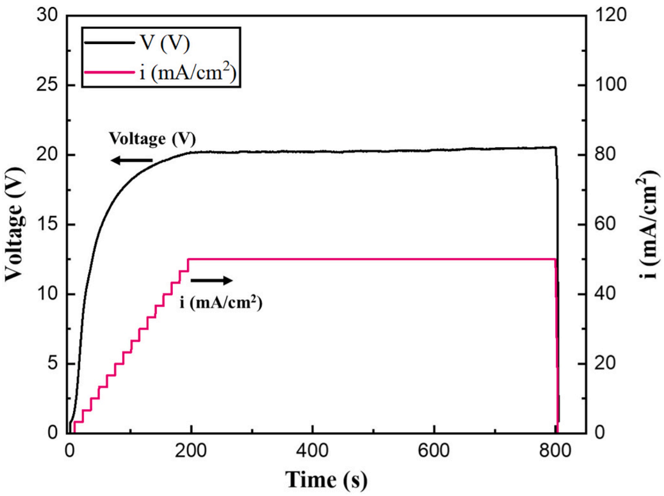

Fig. 2. Current-voltage response of anodizing precursor treatment.

The subsequent electrolytic colouring treatment (Fig. 3(a)), controlled by an RMS voltage of 15 V, results in a different RMS current response depending on the metal deposited (Sn, Cu, or Ni). In the Sn colouring, a significant increase in the current signal is observed during the initial voltage ramp, manifested as two consecutive current peaks. After reaching the set voltage, the current stabilizes at lower values for the remainder of the treatment. A similar behaviour is observed for the Ni colouring, with the initial current increase being less pronounced. In the case of Cu colouring, the current increases progressively and unevenly over time, reaching maximum values between 80 and 100 $\mathrm{mA\cdot cm^{-2}}$. The average current determined for the Sn, Cu, and Ni colouring treatments was 13.70 $\mathrm{mA\cdot cm^{-2}}$, 40.12 $\mathrm{mA\cdot cm^{-2}}$, and 12.29 $\mathrm{mA\cdot cm^{-2}}$, respectively. For Cu, the average current is up to ~3 times higher than that observed for the other deposited metals. Fig. S1 shows the instantaneous voltage and current waveforms corresponding to the different colouring treatments after 200–300 s.

Similarly to the current responses, significant differences are observed in the amount of gas evolved normalized by area throughout the electrolytic colouring treatments (Fig. 3(b)). It should be noted that the entire volume of gas consists of a mixture of H_2 and O_2, resulting from the reduction of H^+ (HER, hydrogen evolution reaction) and H_2O oxidation (OER, oxygen evolution reaction) respectively. Sn and Ni coloured specimens exhibited a pronounced increase in gas volume through the first 100–120 s, coinciding with the observed current peaks. After current stabilization, gas evolution continues at a slower and moderate rate. In contrast, the gradual current rise during the Cu colouring process is reflected in a progressive growth in gas evolution, which leads to a significantly greater amount of gas (~ 0.44 $\mathrm{mL\cdot cm^{-2}}$) compared to the other samples (~ 0.001–0.002 $\mathrm{mL\cdot cm^{-2}}$).

The fundamental electrochemical reactions involved in the colouring process are essentially the same for Ni, Sn and Cu, although their kinetics differ. Variations in current response and gas evolution reflect these kinetic differences, indicating distinct electrochemical behaviours of the deposited metals. During the cathodic pulses, metal ions ($\mathrm{Me^{n+}}$) from the electrolyte are reduced, with deposition occurring predominantly at the pore bottoms and, to a lesser extent, on the pore walls [34,35]. Simultaneously, the HER takes place, leading to the formation of hydrogen bubbles. Conversely, during anodic pulses OER occurs. An increase in current density and continuous gas release can thus be associated with the intensification of these reactions, resulting in enhanced metal deposition and accelerated gas evolution.

Cu, in particular, shows a strong tendency to be reduced ($E_{\mathrm{Cu^{2+}/Cu}}$: +0.34 V vs SHE), while its $\mathrm{Cu^{2+}}$ ions are relatively stable in aqueous

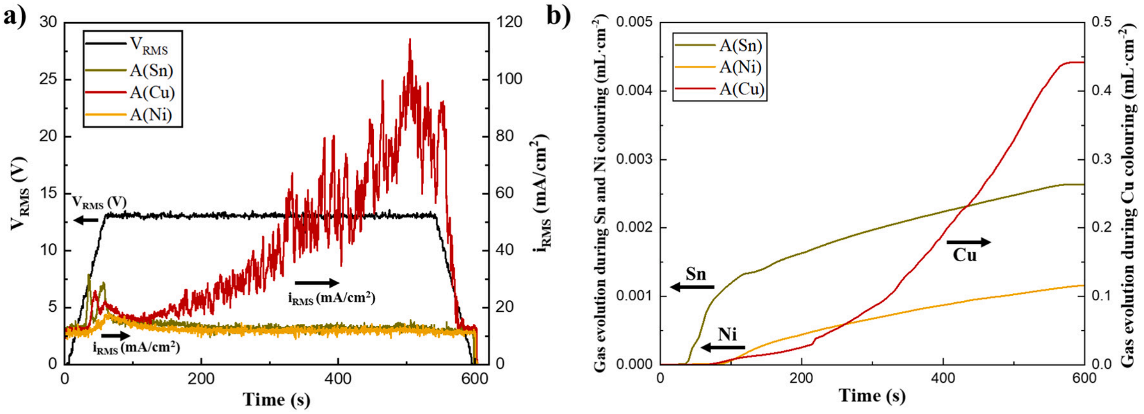

Fig. 3. a) RMS current-voltage response of electrolytic colouring of Sn, Cu and Ni; b) gas evolution normalized by area (~ 3 cm^2) (H_2 and O_2) over time for the different electrolytic colouring treatments.

media. The acidic electrolyte with high conductivity (~ 62 mS/cm) further promotes metal deposition [36]. SEM micrographs at high magnifications illustrated in the following section confirm the incorporation of Cu into the porous structure. Additionally, large metallic agglomerates (diameter ~ 1–3 μm) are observed in the inner regions, suggesting localized rupture of the barrier layer. These ruptures facilitate current passage, providing an additional mechanism that accelerates the deposition process. The greater contribution of the cathodic pulse (Fig. S1) further confirms the enhancement of Cu deposition. During this pulse both metal deposition and hydrogen evolution occur simultaneously.

In the case of Sn colouring, the two initial current peaks observed during the first 100 s indicate Sn deposition within the porous layer accompanied by gas evolution. However, as the current subsequently decreases and stabilizes, the electrochemical reactions become increasingly restricted, making metal deposition less favourable. Previous studies have investigated the mechanisms of Sn electrodeposition and the origins of its relatively low efficiency [37,38]. In acidic electrolytes, Sn^{2+} readily undergoes oxidation, leading to the precipitation of tin oxides (SnO, SnO_2) within the pores. These wide-band-gap semiconductor oxides, characterized by low electrical conductivity, obstruct current flow through the coating and consequently limit both metal reduction and gas evolution during the later stages of treatment.

The response observed during Ni colouring is similar to that of Sn, suggesting an analogous electrochemical behaviour. Therefore, it is reasonable to assume that metal deposition is relatively limited. This limitation may arise from the low ionic conductivity of the electrolyte (~ 9.3 mS/cm).

The amount of metal deposited after the electrolytic colouring treatments was: ~ 1.21 $mmol \cdot cm^{-2}$ for Sn, ~ 9.85 $mmol \cdot cm^{-2}$ for Cu, and ~ 2.35 $mmol \cdot cm^{-2}$ for Ni (values corresponding to an area of 50 cm^2). As discussed throughout this section, the amount of metallic Cu deposited is significantly higher than that of Sn and Ni. In particular, it is ~8 higher than the amount deposited during Sn colouring and ~ 4 higher than that deposited during Ni colouring.

3.2. Voltage-current responses during PEO

RMS current responses through PEO processing (Fig. 4(a)) reveal a characteristic current drop, corresponding to the uniform establishment of the soft sparking regime across the entire surface. This drop coincides with the reaching of the predefined RMS voltage limit as shown in Fig. S2. The RMS current drop times vary depending on the PEO coating, ranging from a maximum of 2400 s for the conventional PEO to a minimum of 950 s for the A(Cu)-PEO. The grey-white appearance of A, PEO and A-PEO treatments contrasts with that of those anodic films containing Sn, Cu and Ni, which vary from bronze to dark purple and light red, respectively. Nonetheless, PEO processing of the metal-containing precursors diminishes their colour intensity, with A(Cu)-PEO remaining the darkest of the three (Fig. 4(b)). A more detailed description of the colour of the PEO coatings is presented in the following section.

The instantaneous response of the voltage and current waveforms for the PEO, A-PEO and A(Cu)-PEO systems at different treatment times is provided as supplementary material (Fig. S3). A detailed explanation of the events occurring during the anodic and cathodic pulses can be found in our previous work [10]. The main differences between the precursor and precursor-free systems are observed in the current response. From the beginning of the treatment, A-PEO and A(Cu)-PEO) exhibit a larger anodic current peak compared with the PEO system (~ 3400 $mA \cdot cm^{-2}$ vs. ~ 1000 $mA \cdot cm^{-2}$). This is attributed to the more intense and longer lasting discharges favoured by the already present thick coating layer. Note that, with time, the PEO system eventually shows a larger anodic peak current due to coating thickening and favoured conditions for stronger discharges [39]. In case of the cathodic pulse, a lower negative charge is observed for precursor-based systems, which is due to the increased impedance of the coating, possibly linked to the entrapment of hydrogen gas bubbles inside the pores of the precursor. This is also a feature that is observed for the PEO system after protracted times.

The evolution of gas generated normalized by area during the PEO treatments is presented in Fig. 5. In all cases, an exponential increase in gas volume is detected during the first 60 s (S_1), coinciding with the current and voltage ramp. The released gases, primarily hydrogen and oxygen in varying proportions, originate from both Faradaic and non-Faradaic processes, including thermal decomposition of water at high temperatures within plasma discharge channels [40,41].

For the specimen subjected to conventional PEO treatment without a precursor layer, there is a sharp increase after 60 s and the gas evolution

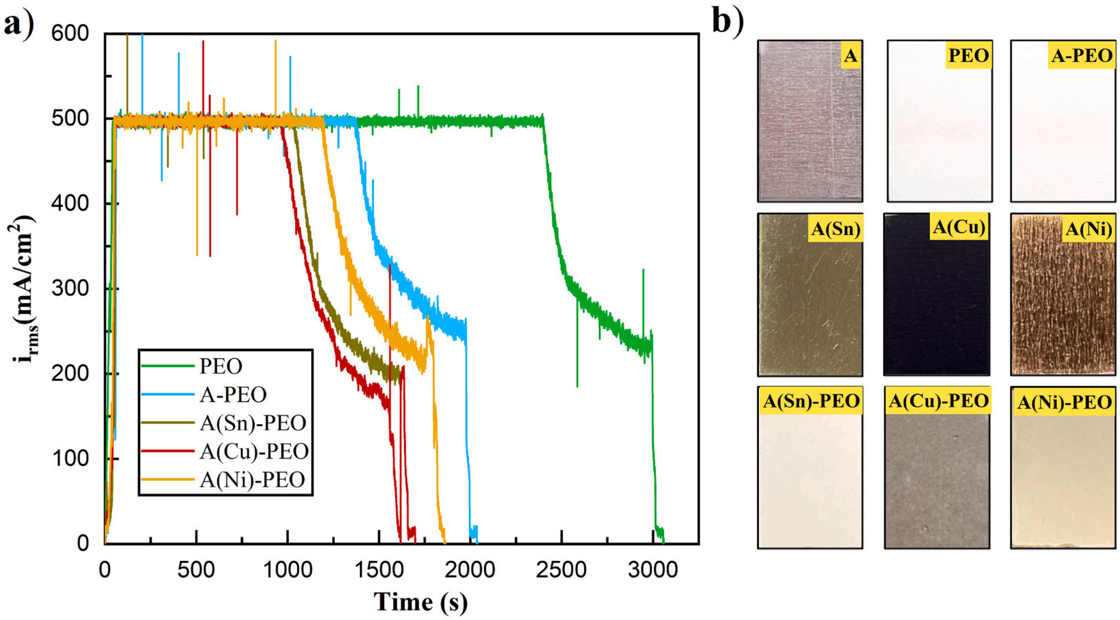

Fig. 4. a) RMS current-time response of different PEO specimens with or without precursor systems; b) surface appearance of precursors and PEO systems. For colour distinction, refer to the online version of this article.

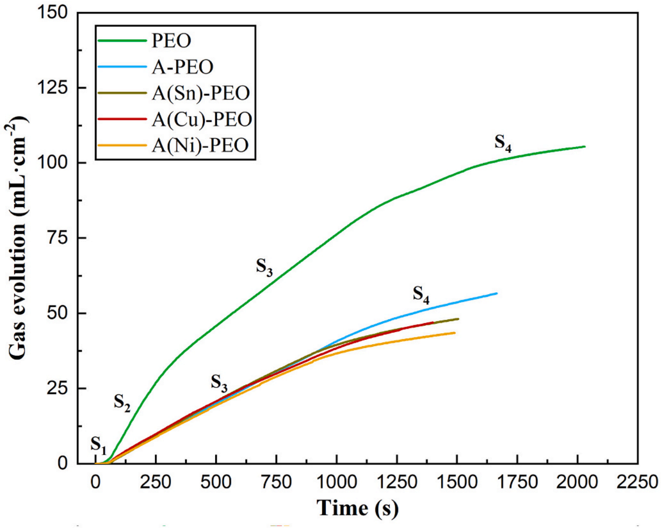

Fig. 5. Gas evolution (H_2 and O_2) normalized by area over time for the different PEO treatments. For colour distinction, refer to the online version of this article.

shows a higher evolution rate during the first ~350 s (S_2). This stage S_2 can be attributed to the development of stronger discharges, which have been suggested to promote anomalous gas evolution through electrolyte decomposition by radiolysis and thermal decomposition, as well as by interaction of water with aluminium microparticles at high temperature [40,42,43]. "Hard microdischarges", characterized by high acoustic emission, occur at these early stages of the process. Note that no soft sparking is observed in the PEO during this time. Subsequently, a slight reduction in gas evolution is detected (S_3). This transition is attributed to the onset of the soft sparking regime. Microdischarges associated with soft sparking initially occur along the specimen edges and in small isolated regions (islands). Although Rogov et al. [44] did not measure gas evolution kinetics, they reported that the transition to this regime is accompanied by a change in gas composition, namely a marked decrease in the proportion of oxygen. This reduction in gas release rate does not affect the measured current, which remains stable over time (not included here for the specimens used in the gas evolution measurements). This indicates that, to maintain a constant current, other electrochemical reactions contributing to ionic current are favoured as the electronic current from oxygen evolution diminishes [44]. Under these conditions, oxide layer growth is sustained by the migration of Al^{3+} and O^{2-} ions, generated through metal oxidation and water dissociation, respectively. A second, less pronounced transition in gas evolution (S_4) becomes evident at longer treatment time (~ 1400 s). This stage corresponds to the uniform establishment of soft sparking across the entire surface and coincides with the characteristic current drop associated with the oxide layer thickening (~ 110 μm) and the consequent increase in coating resistance [45]. Note that the overall treatment time is shorter due to electrolyte heating and lack of stirring (electrolyte agitation was avoided in order to better collect the evolved gas).

The use of a precursor layer results in a significantly lower gas output (~2 times lower) compared to direct PEO, without the S_2 region and showing linear trends (S_3) from the very beginning of the treatment in all cases and without significant differences among Cu, Sn, and Ni. This is attributed to the early establishment of the soft sparking regime along the edges and also as islands across the surface. At longer treatment times, a decrease in gas evolution, similar to that observed in the PEO system, becomes evident. This behaviour is associated with the current drop and the uniform establishment of the soft sparking regime. The overall reduction in gas evolution observed for the precursor systems appears to be associated with a suppressed OER and the limited HER during the cathodic pulse as described for Fig. S3. Further investigation is required to confirm this interpretation.

The specific energy values of anodizing, electrolytic colouring, and PEO treatments are given in Table 2. The total energy consumption is the sum of each energy term normalized by the final coating thickness. The obtained results evidence the positive effect of the precursor systems on the energy consumption of the PEO process. The application of an anodizing layer resulted in ~36 % energy savings, in good agreement with previous studies [45]. Electrolytic colouring significantly enhanced the energy savings, the A(Cu) precursor system yielding the highest value (~ 54 %), mainly due to the early and uniform establishment of soft sparking across the surface. The premature establishment of this regime results in an energy saving of ~18 % for the A(Cu) system compared with the pre-anodized layer (A). The growth rate (μm·min^{-1}) was calculated as the ratio of the final thickness to the total treatment time. Precursor-based systems showed an enhanced growth rate compared to conventional PEO (2.2 μm·min^{-1}), following the order from highest to lowest: A(Cu)-PEO > A(Sn)-PEO > A(Ni)-PEO > A-PEO. All specimens exhibited similar thicknesses (~ 110 μm), as well as comparable surface roughness values (S_a ~ 6–7 μm y S_{10z} ~ 50–70 μm).

3.3. *Characterization of the precursors and PEO coatings*

The colour characterization of the coatings, based on the L*, a*, and b* parameters, is presented in Fig. 6, according to the CIELAB colour sphere. All the precursor systems underwent a change in hue after the colouring treatment. The L* values recorded in all cases exhibit low lightness (L* ≈ 30), which is normally associated with dark or black hues [46]. A(Sn) and A(Ni) systems show similar a* and b* values, characteristic of yellow and red shades. In contrast, A(Cu) system shows a dark purple hue.

Regardless of the precursor, all the PEO coatings exhibit similar colours. In all cases, the recorded L* values are high (L* ≈ 65–85) and the a* and b* values are close to zero, which are associated with white and soft hues. Only the A(Cu)-PEO coating shows a slight indication of yellow hues (b* = 9.4), probably attributed to the dark shade of the original Cu-coloured precursor layer.

SEM cross-sections of the 20 μm precursor coatings are shown in Fig. 7. In all cases, the compositional EDS analysis identifies the presence of Al and O, corresponding to the alumina porous layer, with no morphological irregularities. Additionally, small amounts of S, derived from the acidic electrolyte bath, are also detected. The anodized layer does not exhibit cracking or irregularities in the surface, as indicated in

Table 2
Specific energy consumption of precursor and PEO treatments and total energy consumption. Thickness and roughness parameters of the PEO coatings produced with different precursor systems.

Treatment	E_A	E_C	E_{PEO}	E_{TOTAL}	Growth rate	Thickness	S_a	S_{10z}
	(kWh·m^{-2})			(kWh·m^{-2}·μm^{-1})	μm·min^{-1}	μm		
PEO	–	–	1225	11.0	2.2	111 ± 2	7 ± 1	69 ± 11
A-PEO	1.9	–	772	7.1	3.2	109 ± 2	6.8 ± 0.5	56 ± 3
A(Sn)-PEO	1.9	0.3	597	5.4	4.0	110 ± 1	6.0 ± 0.4	50 ± 5
A(Cu)-PEO	1.9	1.0	564	5.1	3.9	109 ± 1	7 ± 1	54 ± 6
A(Ni)-PEO	1.9	0.3	608	5.6	3.5	108 ± 2	6.5 ± 0.6	54 ± 7

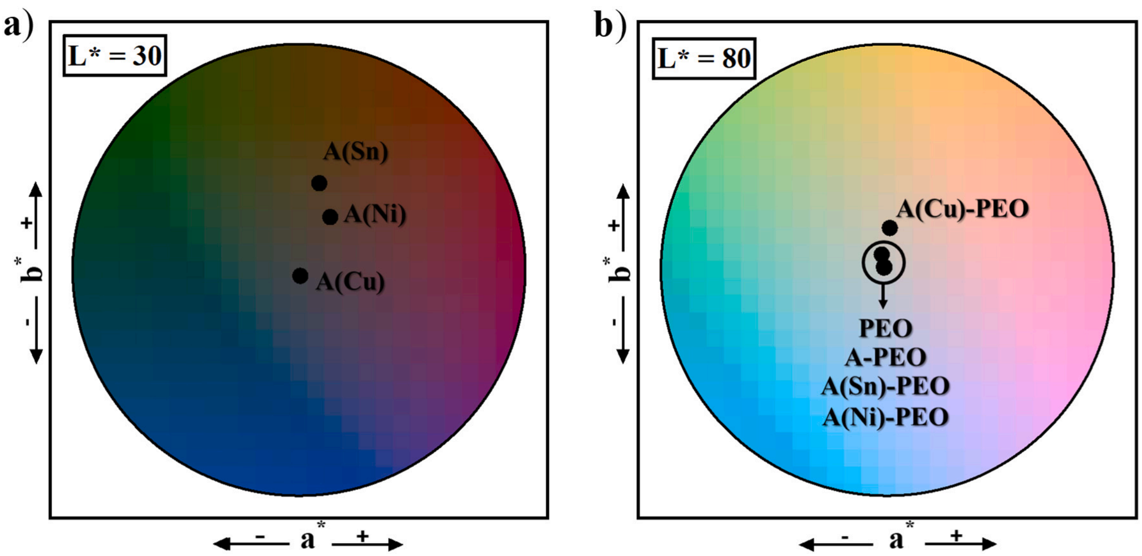

Fig. 6. CIELAB colour sphere a*- b* planes at a lightness (L*) value of: (a) 30 (precursor systems) and (b) 80 (PEO systems).

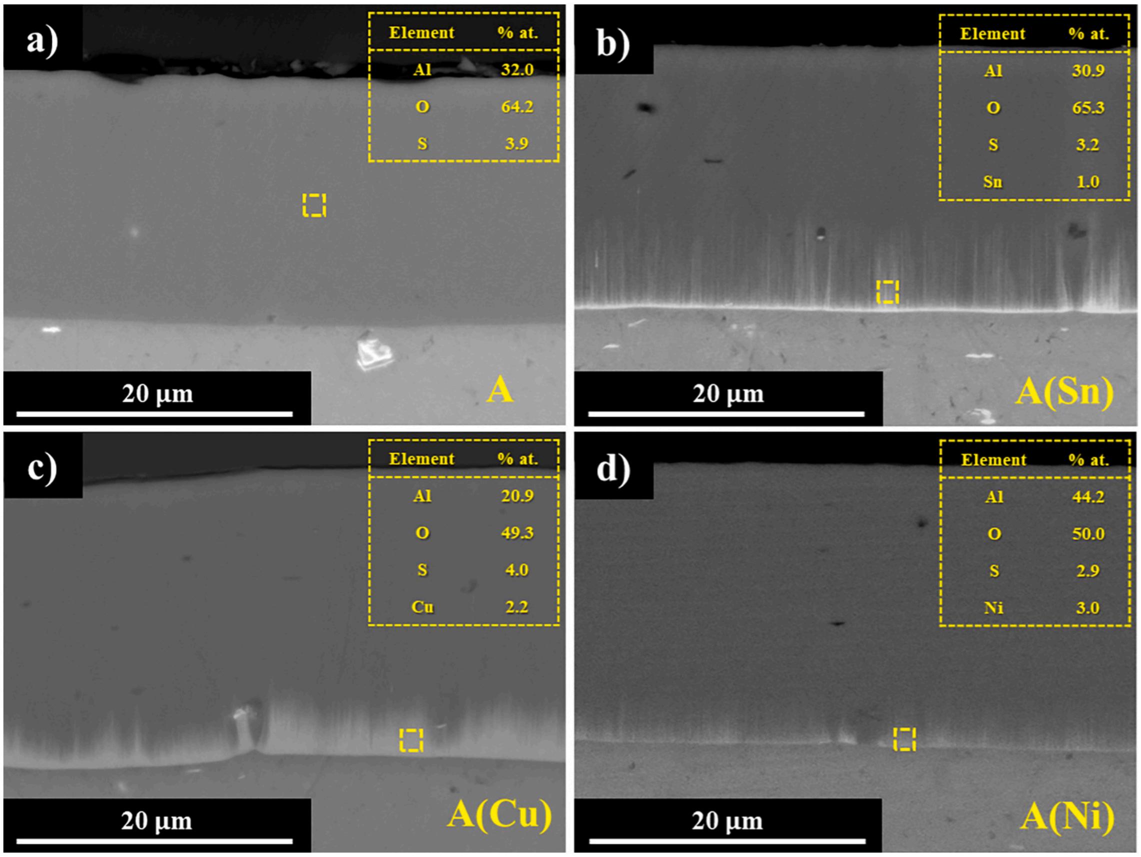

a)

Element	% at.
Al	32.0
O	64.2
S	3.9

b)

Element	% at.
Al	30.9
O	65.3
S	3.2
Sn	1.0

c)

Element	% at.
Al	20.9
O	49.3
S	4.0
Cu	2.2

d)

Element	% at.
Al	44.2
O	50.0
S	2.9
Ni	3.0

Fig. 7. SEM micrographs of precursor systems: (a) anodizing and (b–d) anodizing with electrolytic colouring of Sn, Cu or Ni.

Fig. S4. After the colouring treatment, the incorporation of the respective metals at the inner region of the anodic film is observed. As previously noted, the amount of deposited metal depends on the colouring treatment, following the order: Cu > Sn > Ni. The contrast provided by the electrodeposited metal (Fig. 8) allows for the measurement of the average pore diameter (56 ± 4 nm; average of 5 independent pores measured with ImageJ software). The colouring process does not cause any significant changes in the morphology or thickness of the anodic layer.

SEM plan-view images of the different PEO coatings are shown in Fig. 9. All cases exhibit the typical morphology of PEO layers, with microcracks and pores of various sizes, resulting from thermal stresses and gas evolution, respectively [2,47]. The external porous layer and the intermediate dense layer are clearly distinguishable in the cross-sections. High-magnification images (Fig. S5) suggest a barrier layer thickness ranging from 400 to 600 nm. Additionally, characteristic discharge channels are also visible (Fig. 9(i–f)). The EDS analysis reflects the incorporation of Si, P, Na, and K species from the electrolyte into the

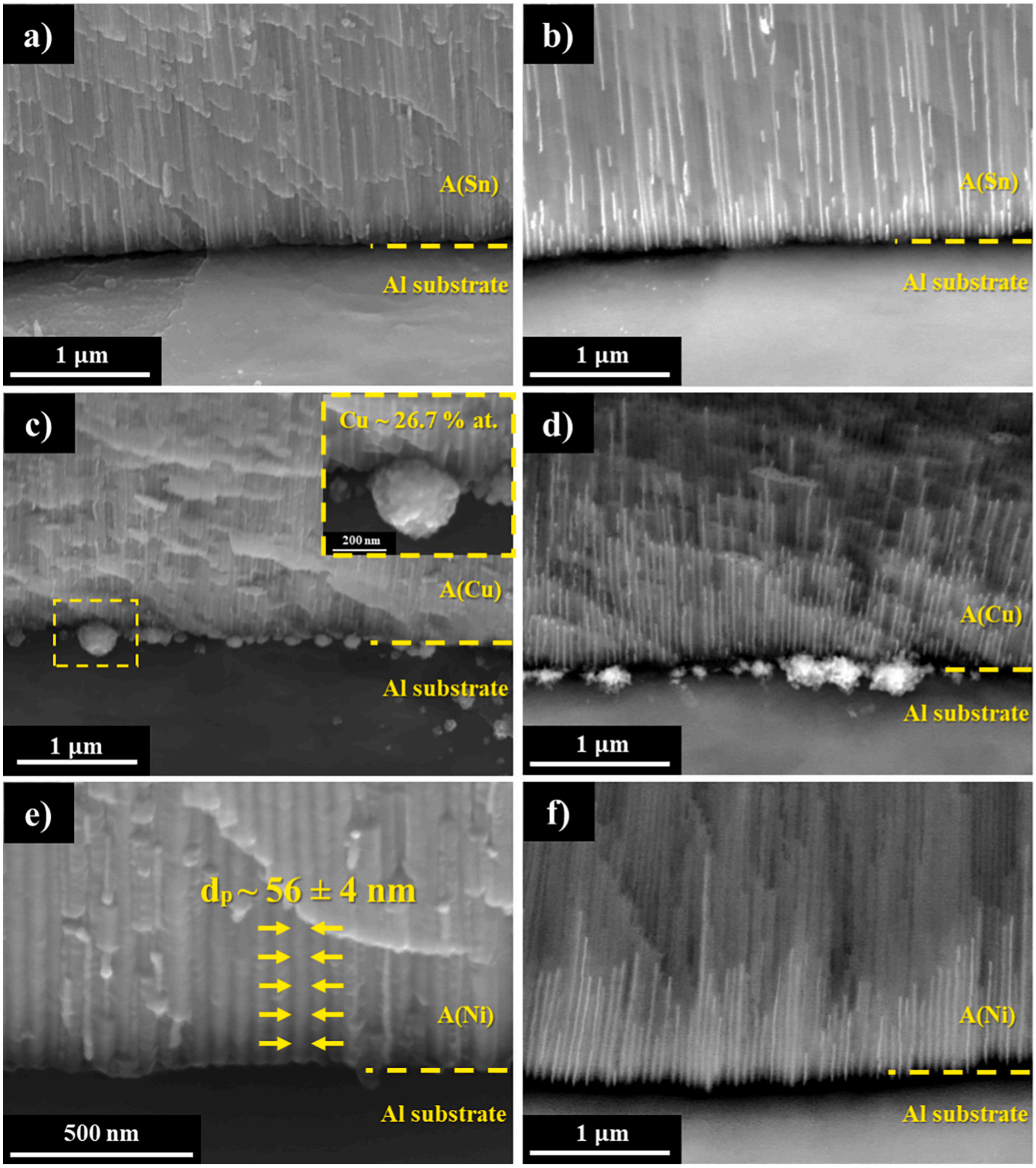

Fig. 8. Higher-magnification SEM micrographs of the precursor systems: (a–b) A(Sn), (c–d) A(Cu) and (e–f) A(Ni). These cross sections correspond to specimens fractured after immersion in liquid nitrogen.

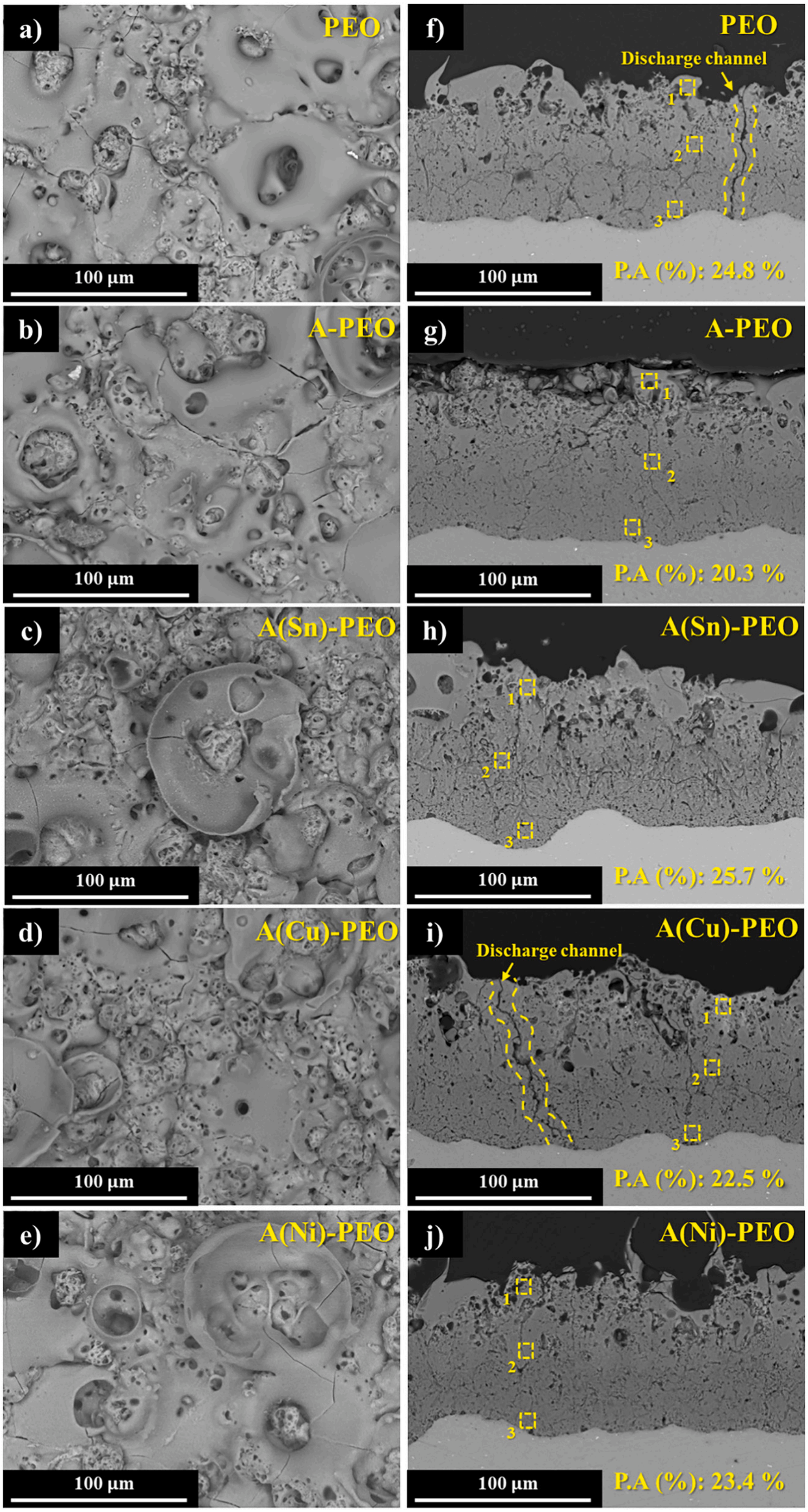

Fig. 9. SEM plan views (a–e) and cross-sections (f–j) micrographs of PEO coatings. (EDS results shown in Table 3.) The "discharge channel" labels highlight vertically aligned cracks that originate from thermal stresses during quick solidification of coating material at the location of the discharge channels.

surface (Table 3). In the precursor systems there is a significant loss of the metals from electrolytic colouring, with less than 1 % detected in the external porous layer. This indicates the release of Sn, Ni and Cu into the electrolyte as a result of the material loss during the discharge [48].

The porosity area percentage of the coating was quantified from SEM cross-sectional images in Fig. 9. Thresholded images highlighting the pores and microcracks are included in Fig. S6. A-PEO system (P.A ∼ 20.3 %) showed slightly higher compactness, consistent with previous studies on anodized precursor systems [10]. This improved compactness compared with the other precursor-based PEO systems is attributed to

Table 3
EDS analysis (at.%) of the PEO coatings obtained from the SEM micrographs, corresponding to Fig. 9.

Sample	Coating zone	Al	O	Si	P	Na	K	Sn	Cu	Ni
PEO	Plan-view[a]	20.0	65.4	10.4	0.6	1.8	1.9	–	–	–
	(1) External	18.0	55.4	6.3	0.4	0.3	0.5	–	–	–
	(2) Middle	26.4	63.4	8.9	0.8	0.1	0.5	–	–	–
	(3) Internal	37.0	59.7	1.7	1.0	0.2	0.4	–	–	–
A-PEO	Plan-view[a]	19.7	65.6	9.8	0.9	2.3	2.2	–	–	–
	(1) External	19.0	60.4	15.3	0.5	1.7	2.8	–	–	–
	(2) Middle	28.5	62.6	7.7	0.4	0.3	0.6	–	–	–
	(3) Internal	37.0	60.7	1.6	0.6	0.7	0.2	–	–	–
A(Sn)-PEO	Plan-view[a]	19.2	66.6	9.6	0.6	1.6	2.2	0.2	–	–
	(1) External	26.7	65.8	6.5	0.3	0.3	0.4	0.1	–	–
	(2) Middle	32.5	65.5	1.5	0.3	0.1	0.2	–	–	–
	(3) Internal	38.7	59.8	0.8	0.4	0.2	0.1	–	–	–
A(Cu)-PEO	Plan-view[a]	18.0	64.0	10.9	0.9	3.3	2.8	–	0.3	–
	(1) External	16.8	60.1	14.0	0.7	0.4	4.5	–	1.2	–
	(2) Middle	35.0	60.7	3.2	0.5	2.8	0.3	–	0.1	–
	(3) Internal	36.6	61.6	0.9	0.6	0.2	0.2	–	–	–
A(Ni)-PEO	Plan-view[a]	21.0	66.1	9.7	0.4	1.0	1.8	–	–	0.1
	(1) External	23.8	63.2	10.6	0.7	0.5	1.1	–	–	0.1
	(2) Middle	35.9	61.7	1.5	0.2	0.3	0.2	–	–	0.2
	(3) Internal	36.5	60.3	1.7	0.9	0.2	0.3	–	–	–

[a] EDS analyses of the plan-view micrographs correspond to the entire surface of the image.

the longer treatment and exposure to the soft sparking regime (Fig. 4), which promotes the formation of denser coatings with smaller pore sizes compared with those formed under arc conditions [27].

The XRD patterns of the precursor coatings (Fig. 10(a)) reveal the amorphous nature of the conventional anodic layers. After the electrolytic colouring process, distinct XRD peaks corresponding to metallic Ni (ICDD: 00-001-1260) and Cu (ICDD: 01-085-1326) are observed. In the case of Sn-colouring, the detected peaks were assigned to Sn(II, IV) oxides (ICDD: 00-001-0891, 00-029-1484). Previous XPS studies under similar conditions have confirmed the coexistence of both SnO and SnO_2 species [37]. No clear peaks corresponding to metallic Sn are detected, likely due to either (i) the low amount of Sn deposited at the base of the layer or (ii) oxidation of the metal during or after deposition. In either case, the presence of tin oxides in the coating supports the earlier discussion on the current and gas evolution responses observed during Sn-colouring.

Fig. 10(b) shows the presence of α-Al_2O_3 (ICDD: 01-074-1081), γ-Al_2O_3 (ICDD: 00-047-1308), and mullite (ICDD: 00-079-1450) phases in all PEO coatings. The formation of phases such as α-Al_2O_3 and mullite, which contribute to excellent mechanical properties, results from the high temperatures generated by microdischarges and the extended treatment times [49]. As observed in the precursor layers, peaks corresponding to the Al substrate (ICDD: 00-001-1176) are also detected. No additional phases are identified for the different precursor systems.

The crystallinity index (C.I.) of each coating was estimated as the ratio between the sum of the integrated relative intensities of the crystalline peaks and the total sum of the intensities in the spectrum, including both amorphous and crystalline contributions. All specimens exhibit similar C.I. values, approximately 0.30–0.35, indicating the presence of significant amounts of amorphous material, which appears as a broad peak in the 15–40° range. This amorphous fraction is mainly located in the outer part of the coating [47].

The ratio of α-Al_2O_3 to γ-Al_2O_3 phases (Fig. 11) was calculated from the relative integrated intensities of the peaks at 43.4° and 45.8°, corresponding to the (113) plane of α-Al_2O_3 and the (400) plane of γ-Al_2O_3, respectively [50]. The α-Al_2O_3/γ-Al_2O_3 ratio for the different PEO systems was as follows: 0.88 PEO, 1.35 A-PEO, 1.13 A(Sn)-PEO, 1.18 A(Cu)-PEO, and 1.25 A(Ni)-PEO. A higher α-Al_2O_3/γ-Al_2O_3 ratio is observed in the A-PEO and A(Ni)-PEO systems (~ 1.35 and 1.25, respectively) compared to the other coatings (~ 0.88–1.18).

The transformation from γ-Al_2O_3 to α-Al_2O_3 is influenced by multiple factors, including the presence of impurities, coating porosity, and oxide conductivity, with no single factor clearly dominating [51]. Nonetheless, it is well established that transition to the soft sparking regime promotes denser coatings and higher α-Al_2O_3 content [52]. The use of

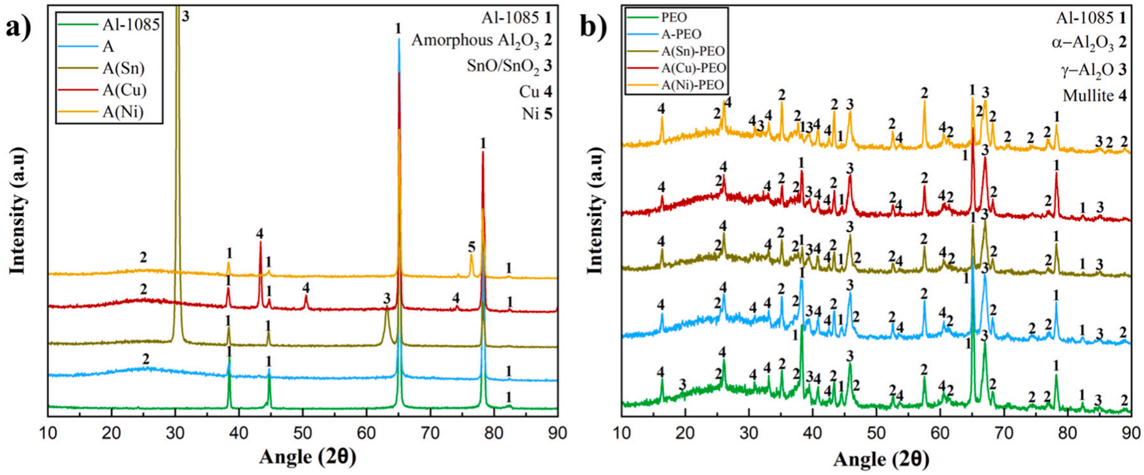

Fig. 10. X-ray diffraction patterns of precursor systems (a) and PEO coatings (b). For colour distinction, refer to the online version of this article.

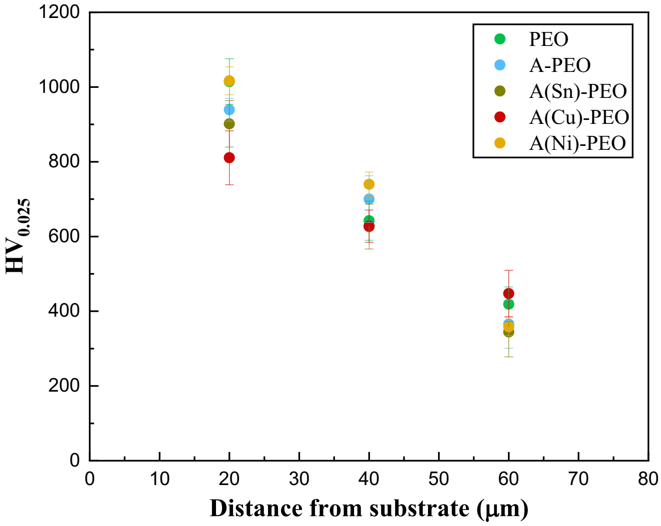

Fig. 11. Microhardness profile of PEO coatings with and without precursor systems. For colour distinction, refer to the online version of this article.

divalent metallic dopants (Me^{2+}) has been explored as a strategy to assist the γ → α phase transition in catalyst and catalyst-support materials. Dopants are typically classified as accelerators, neutral or retardants [53]. Ni^{2+} is generally considered to have minimal influence on this transformation. Therefore, the higher α-Al_2O_3/γ-Al_2O_3 ratio observed in the A-PEO and A(Ni)-PEO systems is likely to be associated with longer treatment times and, therefore, longer exposure to the soft sparking regime (Fig. 4) than to any dopant effect of Ni^{2+} in the alumina film. A similar explanation is plausible for the A(Cu)-PEO system. Despite the reported accelerating effect of Cu in the γ to α transformation [42], it shows a lower α/γ ratio than A-PEO and A(Ni)-PEO possibly due to a shorter period of time under soft sparking (Fig. 4).

Microhardness profiles of the PEO systems, with and without the precursor coating, are shown in Fig. 11. The high hardness achieved in all the cases is attributed to the formation of the α-Al_2O_3 phase, previously identified in the XRD patterns [20]. The highest hardness values correspond to the inner region part of the coating (~ 20 μm). In this region, a higher proportion of the α-Al_2O_3 phase is detected, along with the formation of a more compact coating [5]. A significant decrease in hardness is identified at greater thicknesses relative to the coating/substrate interface (~ 40–60 μm). The reduction in hardness in these zones is associated with a higher proportion of the γ-Al_2O_3 phase and increased porosity. All systems exhibited a similar trend among them, consistent with that reported in previous studies [54]. A-PEO and A(Ni)-PEO showed higher hardness in the inner region of the coating (~ 20–40 μm), which can be attributed to their higher α-Al_2O_3/γ-Al_2O_3 ratio mentioned before.

3.4. *Influence of precursor layers on PEO growth*

Figs. 12, 13, 14 and 15 show electron micrographs of the precursor systems subjected to partial PEO treatment. In all cases, the cut-off times were insufficient for full PEO coating development across the surface, allowing visualization of distinct regions: the precursor layer, the PEO coating, and their transition zone.

Fig. 12 presents cross-sectional SEM micrographs of the A-PEO system. After 200 s of treatment, a porous PEO coating is partially formed in random surface areas (Fig. 12(a)). In regions where PEO did not develop, initial microdischarges are observed within the inner part of the anodized layer (Fig. 12(b)). Across these areas, and within the precursor coating more generally, thickening of the anodic barrier layer

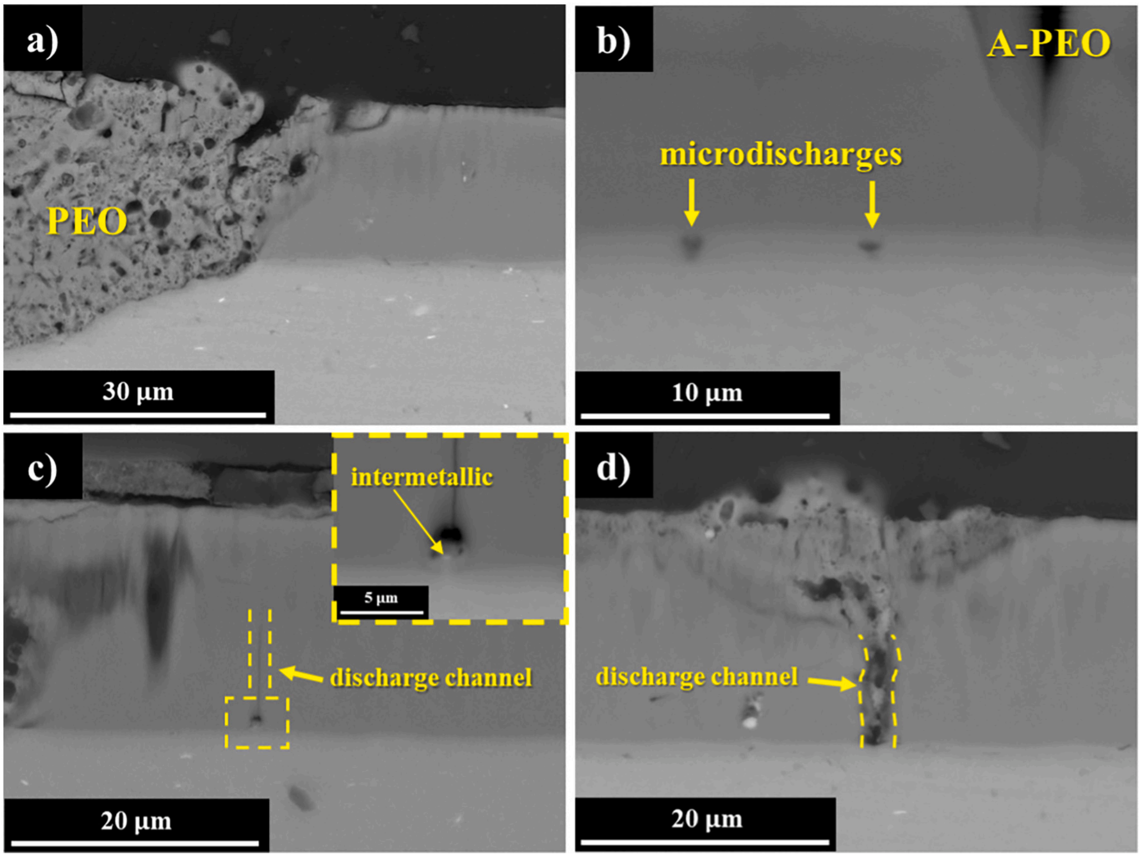

Fig. 12. Cross-section SEM micrographs of the A-PEO coating after 200 s of the PEO treatment.

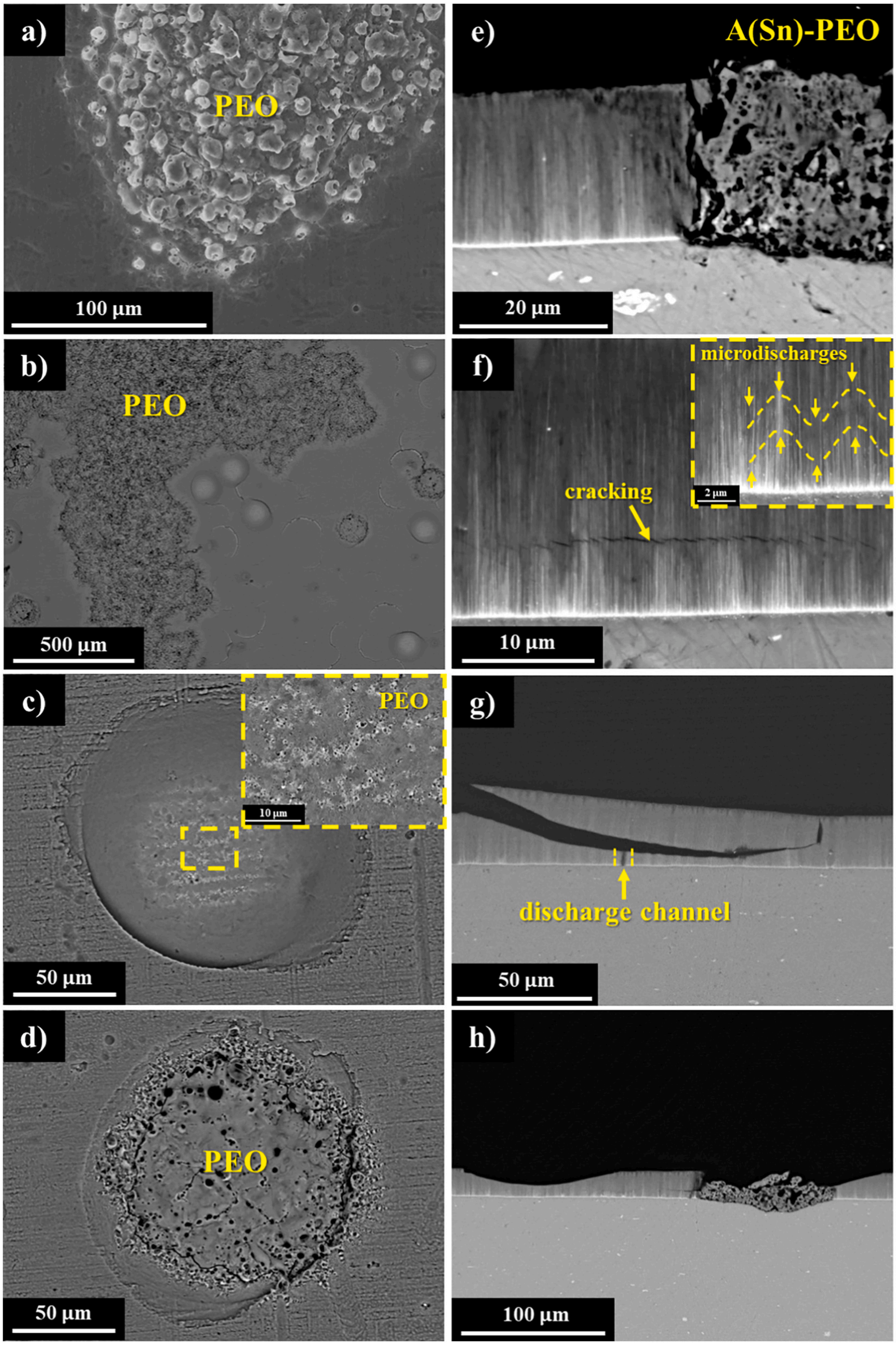

Fig. 13. Plan-view and cross-section SEM micrographs of the A(Sn)-PEO coating with precursor layer A(Sn) after 100 s (a, e, and f) and 200 s (b, c, d, g and h) of the PEO treatment.

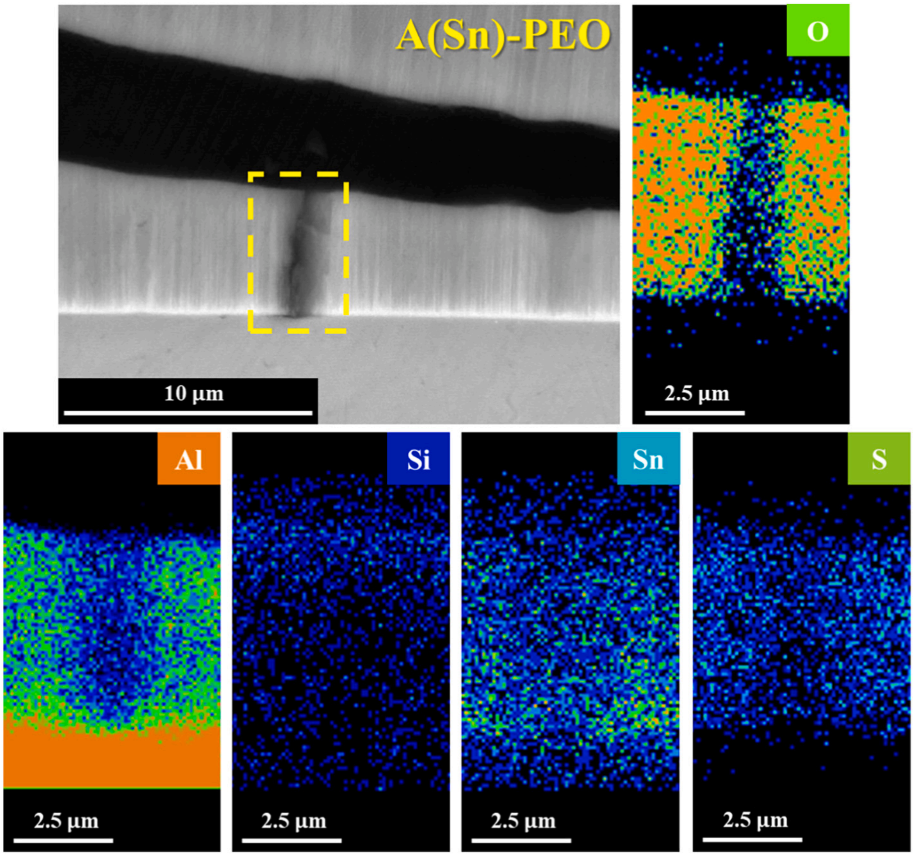

Fig. 14. Cross-sectional SEM micrographs of a discharge channel in the A(Sn)-PEO system and the corresponding compositional maps.

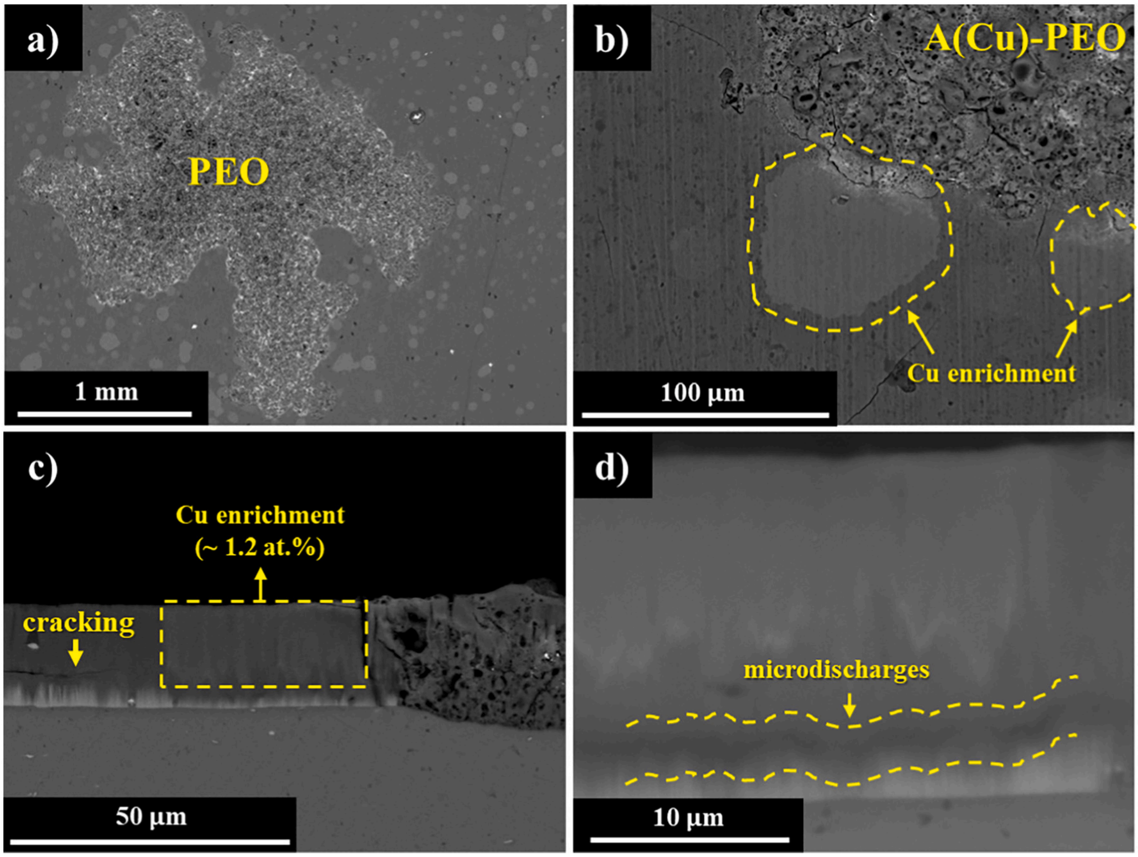

Fig. 15. Plan-view and cross-section SEM micrographs of the A(Cu)-PEO coating with precursor layer A(Cu) after 400 s of the PEO treatment.

occurs, likely due to the high voltages applied during the first seconds of treatment. Initial microdischarges are also detected in regions enriched with intermetallics (Fe ~ 1.5 at.%) (Fig. 12(c)). An example of a more developed discharge channel is visible in Fig. 12(d).

It is well established that microdischarges occur at localized sites under the strong electric field [55]. In the A-PEO system, two main microdischarge sites have been identified: (i) the barrier layer and (ii) intermetallics. Previous studies have reported that approximately 90 % of the electric field is concentrated within the barrier layer, supporting the conclusion that this is the dominant discharge initiation site [56]. Additionally, the intermetallics disrupt the barrier layer and promote local field concentration and subsequent dielectric breakdown of the oxide. However, the frequency of discharge initiation in intermetallic particles is significantly lower than in localized regions of the barrier layer due to their small population density.

Plan-view micrograph of the A(Sn) precursor system after 100 and 200 s of treatment show scattered PEO-coated regions, similar to those observed in the A-PEO system (Fig. 13(a)), and circular features with circumferential cracks (Fig. 13(b)). At higher magnification, early PEO growth is observed within the latter, showing varying degrees of development (Fig. 13(c–d)). With continued growth, these areas transition into the soft sparking regime and were no longer visible.

Cross-sectional image in Fig. 13(e) reveals that the Sn-rich region in the precursor layer gets dispersed within the growing PEO coating material (bright contrast zones). Unlike the A-PEO system, microdischarges originating in the barrier layer of the precursor coating are not observed, likely due to pore filling during electrolytic colouring. Instead, a dark wavemark above the Sn-rich deposit indicates the onset of microdischarges in these regions (Fig. 13(f)). In this case, dielectric breakdown of the oxide layer and gas evolution produce stresses resulting in longitudinal and curved cracks in the coating (Fig. 13(f–g)). This cracking leads to partial oxide detachment, creating semicircular cavities where further PEO growth occurs (Fig. 13(h)). These surface features correspond to those previously identified in the longitudinal micrographs.

Fig. 14 shows a more detailed characterization of a discharge channel in the A(Sn)-PEO system, depicted in Fig. 13(g), along with the corresponding compositional maps.

The Al, O, and S maps are consistent with formation of a wide pore at the site of the breakdown (i.e. lower concentration). The impact of the high temperature of the discharge is also evident in the re-distribution of Sn, which is reduced at the coating/substrate interface. The uniform Al enrichment at the bottom of the pore also indicates re-growth of the barrier layer after the extinction of the discharge. Finally, the slight Si enrichment at the mouth of the pore is consistent with the electrolyte ingress typically observed in PEO processes. Note that this discharge event represents a more advanced stage compared to the smaller discharges that produce the wavemarks as previously discussed.

A similar behaviour is observed in the A(Cu) system (Fig. 15(a, b)). Microdischarges and cracks, although less evident, are observed above the metallic Cu (Fig. 15(c)). Additionally, there are circular features where Cu ascends to the upper regions of the precursor (Fig. 15(b, d)).

The migration of Cu within the precursor layer can be interpreted analogously to the behaviour of alloying elements during PEO. Previous studies have shown that, during oxide growth, alloying elements originally present in the aluminium substrate, either in solid solution or as intermetallics, are incorporated into the coating in ionic form [57]. These species migrate toward the outer coating region, where they may eventually be released into the electrolyte. Their residual concentration within the coating depends on both the chemical nature of the element and its ionic mobility within the oxide. For Cu^{2+}, ionic mobility in amorphous anodic alumina films has been reported to be up to ~3.2 times higher than that of Al^{3+} ions [58]. Based on these considerations, it is reasonable to assume that the high applied voltages and the

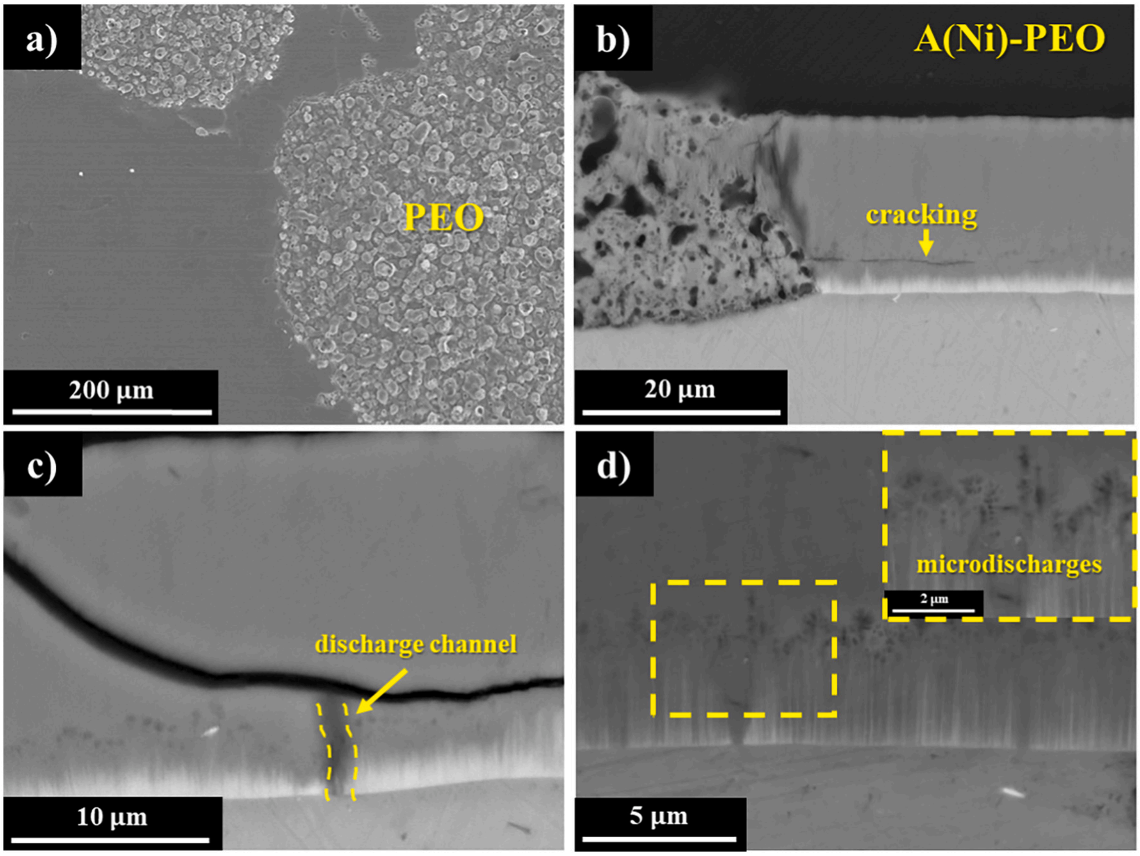

Fig. 16. Plan-view and cross-section SEM micrographs of the A(Ni)-PEO coating with precursor layer A(Ni) after 200 s (a–c) and 30 s (d) of the PEO treatment.

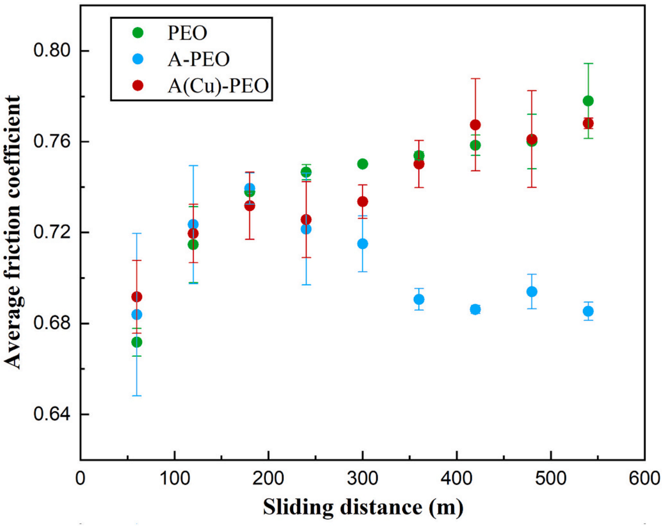

Fig. 17. Variation of the average friction coefficient as a function of the sliding distance of the selected coatings. For colour distinction, refer to the online version of this article.

localized electric fields promote the migration of Cu through the precursor layer, particularly in regions where microdischarges assist the incorporation of Cu into the oxide layer.

Fig. 16 shows the SEM characterization of the A(Ni) system after 30 and 200 s of PEO treatment. Similar to the other cases, PEO grows in islands (Fig. 16(a)) and there is cracking of the precursor layer above the deposited metallic Ni (Fig. 16(b–c)). In addition, the dark wavemark associated with the onset of microdischarges is observed with greater clarity just above the electrodeposited metal. In this case, the breakdown events result in dark regions with a dendritic morphology (Fig. 16(d)).

In summary, electrolytic colouring creates new metal-electrolyte interfaces, where the deposited columns of metal with high electronic conductivity (Sn ~ $9.17 \cdot 10^6$ S/m; Cu ~ $5.96 \cdot 10^7$ S/m; Ni ~ $1.43 \cdot 10^7$ S/m) sustain current flow, acting as conductive bridges rather than allowing field concentration in the barrier layer. Therefore, the top-ends of the metal columns behave analogously to intermetallics, becoming localized sites for discharge initiation, thus promoting an earlier onset of soft sparking. The higher current response during the Cu-colouring process, together with the presence of large metallic deposits in the inner regions of the precursor, indicated a higher quantity of deposited metal compared with Sn or Ni. This and the high electrical conductivity of metallic Cu could explain the earlier onset of soft sparking in this case compared to Sn and Ni.

3.5. *Wear and corrosion behaviour*

The precursor system A(Cu), which provided the highest energy savings, was selected to study its effect on the wear and corrosion behaviour of the resulting PEO coating. The results were compared with those of PEO coatings with and without a precursor layer. The variation of the average friction coefficient over 600 m under a 10 N load for the selected systems is illustrated in Fig. 17. These values are consistent with those reported in previous studies of anodized precursor layers [10]. The amount of removed material corresponds to an approximate depth of ~25 μm, mainly associated with the external porous layer. The wear rate (W_r) expressed in $mm^3 \cdot N^{-1} \cdot m^{-1}$ is $(2.3 \pm 0.3) \cdot 10^{-5}$ for PEO, $(2.1 \pm 0.1) \cdot 10^{-5}$ for A-PEO, and $(2.5 \pm 0.3) \cdot 10^{-5}$ for A(Cu)-PEO.

The results highlight the different behaviour of PEO and A(Cu)-PEO systems compared with A-PEO. The latter exhibits a reduction in the average friction coefficient at sliding distances above 300 m (~ 0.69), which is attributed to its higher compactness and greater proportion of the α-Al_2O_3 phase resulting from the prolonged soft sparking regime. This behaviour is also reflected in W_r, where this parameter is likewise lower.

SEM plan-view images of the wear tracks (Fig. 18) show debris accumulation along the track edges. At higher magnification (Fig. 18 (d–f)), the formation of a tribolayer is evident, with clear signs of cracking caused by stresses induced by the sliding counterpart. EDS analyses of selected areas reveal elements such as Si, Na, P, and K, confirming that wear predominantly affects the external porous regions of the coating. Additionally, significant amounts of W (3–4 at.%) were detected, particularly in brighter regions of the images, indicating damage of the WC counterpart and subsequent transfer of this material to the tribolayer during sliding. As previously reported, the dense, hard and adherent W-rich tribolayer helps to reduce the material loss [5]. The wear debris generated by the PEO and A(Cu)-PEO (Fig. S7, Supplementary Table 1) show a highly irregular and fragmented morphology, typical of brittle fracture. In the A(Cu)-PEO system, a small amount of Cu (~ 0.9–1.3 at.%), derived from the precursor layer, was also detected. These results together with the cracking of the tribolayer shown in Fig. 18 indicate a predominantly three-body abrasive wear mechanism, where the detached fragments act as additional abrasive particles during sliding.

Overall, these results demonstrate that the energy savings achieved

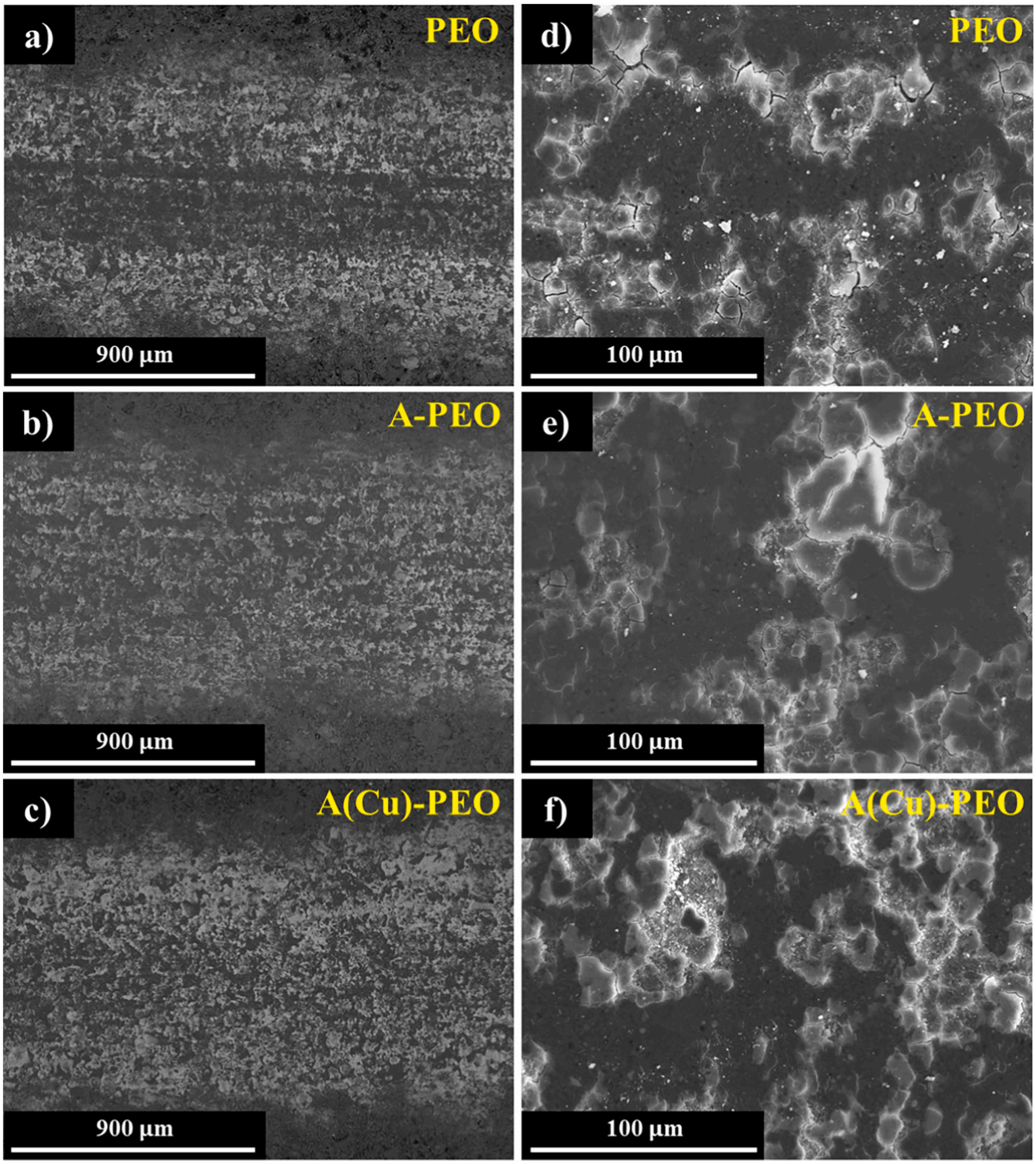

Fig. 18. SEM plan-view of the wear tracks after 600 m under a 10 N load for the different PEO coatings (PEO, A-PEO and A(Cu)-PEO).

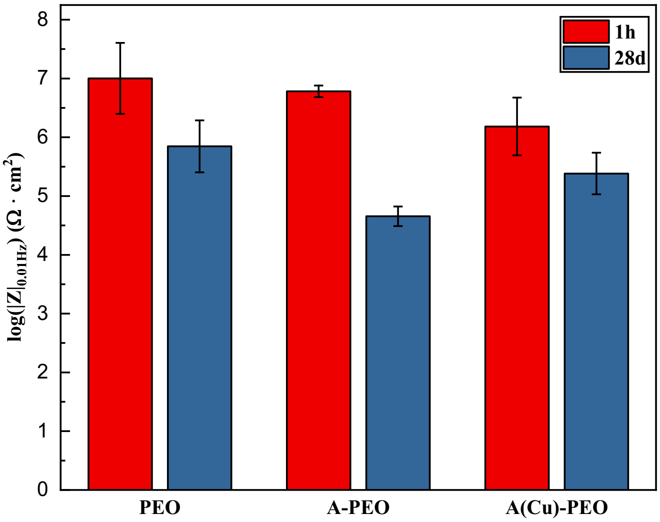

Fig. 19. Impedance modulus of the different PEO coatings after 1 h and 28 days of immersion in a 3.5 wt% NaCl aqueous solution. For colour distinction, refer to the online version of this article.

through precursor systems do not compromise wear resistance.

Fig. 19 shows the impedance modulus (|Z|) at low frequency (0.01 Hz) after 1 h and 28 days of immersion in 3.5 wt% NaCl solution. After 1 h, all systems showed |Z| values above 10^6 Ω·cm^2, with A(Cu)-PEO slightly lower than the other two. However, after 28 days a pronounced decrease in |Z| was observed for all coatings, indicating coating failure due to corrosion.

Bode and Nyquist plots at different immersion times (1 h, 48 h, 7 d, 14 d, and 28 d) are shown in Fig. 20. The experimental spectra were fitted using the equivalent circuit showed in Fig. 21(d), which is a simplified but sufficient representation for comparison of the studied systems. This circuit ignores transitional processes, such as diffusion, that were observed at low frequencies for some specimens. The fittings yielded χ^2 values below 0.01, confirming the robustness of the models. The fitted parameters are summarized in Table 4. R_s corresponds to the electrolyte resistance, which varied between 10 and 60 Ω·cm^2. Over the 28-day immersion period, the systems exhibited three distinct time constants associated with: (i) the porous layer (CPE_{out}/R_{out}), (ii) the intermediate dense layer (CPE_{inter}/R_{inter}), and (iii) the inner or barrier layer (CPE_{in}/R_{in}).

The time evolution of the different resistances associated with each element of the PEO coatings (R_{out}, R_{inter} and R_{in}) is shown in Fig. 21 (a–c). R_{out} (Fig. 21(a)) is significantly lower compared to the other resistances. This is reasonable since, as previously mentioned, it corresponds to the porous region of the coating. As is well known, the highest corrosion resistance is provided by the inner part of the coating, identified as CPE_{inter}/R_{inter} and CPE_{in}/R_{in} in the circuit Fig. 21(d). After 1 h of immersion, the PEO system exhibited a higher R_{out} value ($6.5{\cdot}10^3$ Ω·cm^2) compared to the other cases (A-PEO = $1.2{\cdot}10^3$ Ω·cm^2 and A(Cu)-PEO = $2.0{\cdot}10^3$ Ω·cm^2). With longer immersion times, a significant degradation of R_{out} was observed in all systems. No substantial improvements in this parameter were identified after extended exposure.

A clear difference in R_{inter} (Fig. 21(b)) associated with the dense intermediate layer of the coating was observed during the initial immersion times (1 h and 48 h). The R_{inter} corresponding to A-PEO is significantly higher ($1.2{\cdot}10^5$ Ω·cm^2) than in the other cases (PEO = $3.7{\cdot}10^4$ Ω·cm^2 and A(Cu)-PEO = $2.0{\cdot}10^4$ Ω·cm^2), possibly due its higher compactness. After prolonged immersion times, a significant degradation of R_{inter} was observed in all cases. Depending on the system, a recovery of R_{inter} was identified at different temporal points: at 7 days for the PEO and A(Cu)-PEO systems, and at 28 days for A-PEO. This recovery may be associated with the formation and accumulation of corrosion products within the pores and microcracks in the inner part of the coating [14]. Fig. S8 shows an example of the accumulation of corrosion products in a discharge channel corresponding to the PEO system. Hydrolysed material is identified inside the discharge channel, along with the presence of Cl detected by EDS analysis.

Similar to the previous cases, R_{in} (Fig. 21(c)) shows degradation with time, indicating localized failure of the barrier layer. It is worth noting the lower R_{in} exhibited by A(Cu)-PEO after 1 h of immersion ($4.5{\cdot}10^6$ Ω·cm^2). This is likely related to Cu enrichment in the barrier layer influencing aspects such as crystallinity, defects and electronic conductivity, which require further investigation.

Fig. 22 presents SEM cross-sectional images of the coatings after 28 days of corrosion testing. All systems display discontinuities in the barrier layer, indicating corrosion processes already initiated at the substrate. The limited size of these discontinuities suggests that corrosion remains at an early stage under the present exposure conditions. EDS analyses indicate the presence of Cl (1–2 at.%) within the cavities and along the discharge channels, confirming the penetration of the corrosive medium. The oxygen compositional map of the PEO coating (Fig. 22(b)) discloses lack of O within these cavities, further supporting the evidence of barrier layer failure through its dissolution. The formation of corrosion products becomes evident in the inner regions of the coating, as shown by the Al and Cl compositional maps corresponding to the PEO (Fig. 22(c, d)). The increase in Cl in the inner regions coincides with the reduction of Al content. The contrast between these two elements suggests the dissolution of exposed Al and the formation of hydrolysed material.

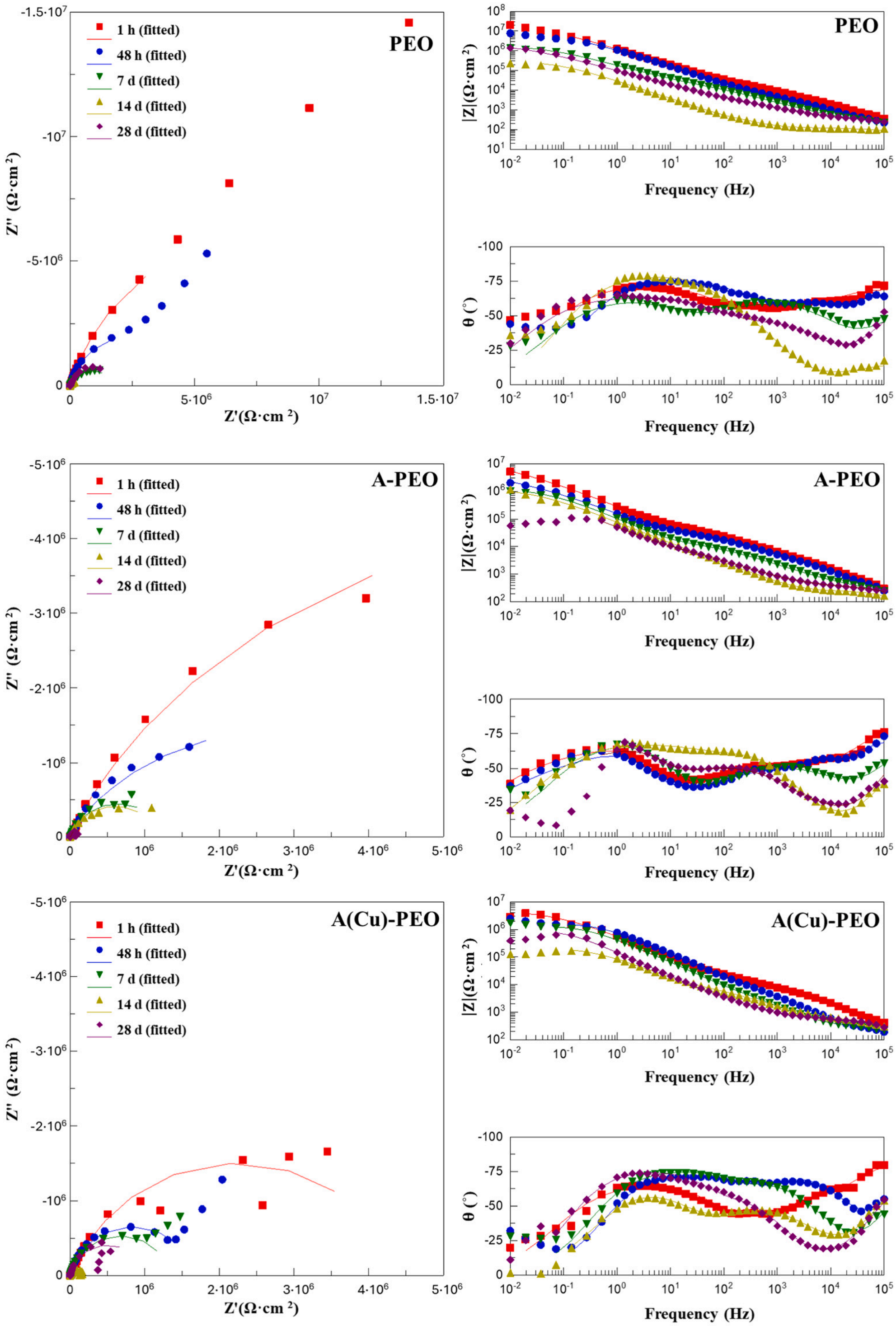

Fig. 20. Bode and Nyquist diagrams at 1 h, 48 h, 7 d, 14 d, and 28 d of immersion in 3.5 wt% NaCl of the systems: a) PEO, b) A-PEO, and c) A(Cu)-PEO.

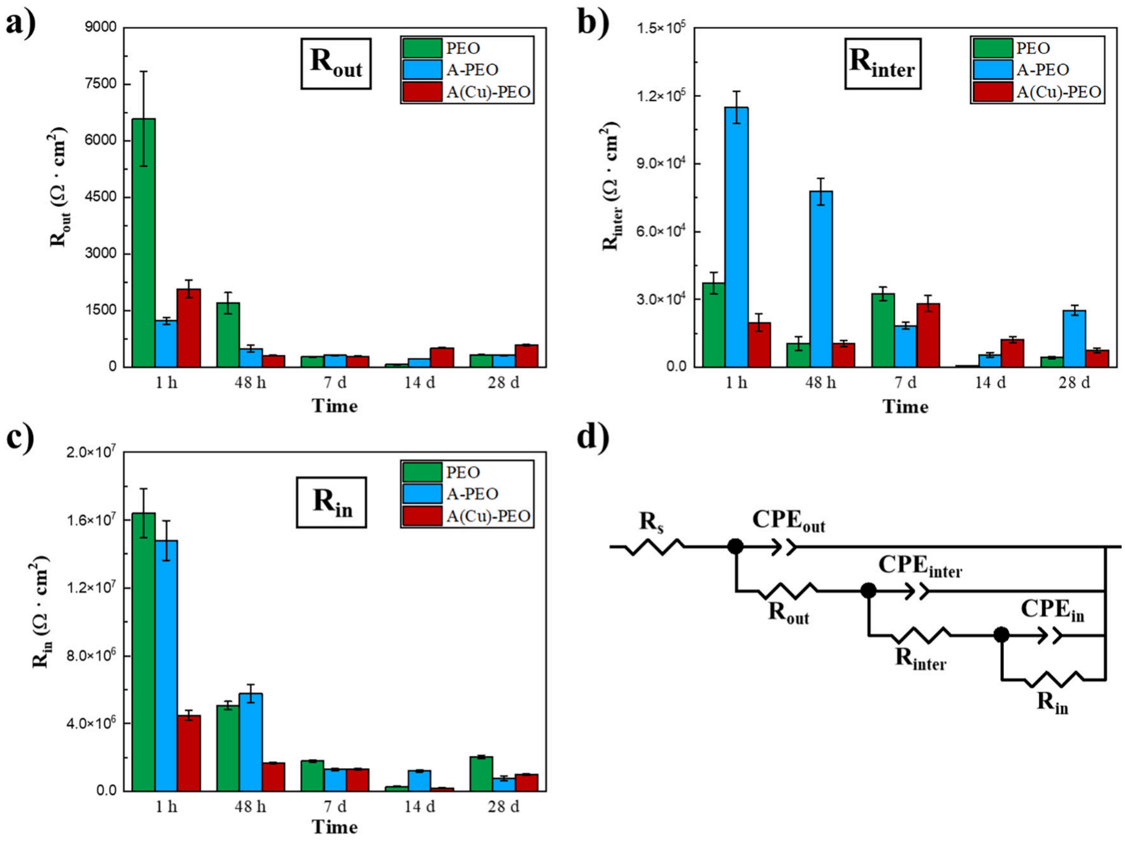

Fig. 21. a–c) Time evolution of R_{out}, R_{inter} and R_{in} during 28 days of immersion in 3.5 % NaCl and d) equivalent circuit used for fitting the selected PEO systems. For colour distinction, refer to the online version of this article.

Table 4

Fitting results of the equivalent electrical parameters for PEO, A-PEO, and A(Cu)-PEO systems. $R_{out/inter/in}$, $\Omega\cdot cm^2$; CPE $_{out/inter/in}$, $S\cdot s^n\cdot cm^{-2}$.

Time	CPE_{out}	n	R_{out}	CPE_{inter}	n	R_{inter}	CPE_{in}	n	R_{in}	χ^2
PEO										
1 h	$4.5\cdot10^{-8}$	0.82	$6.5\cdot10^{3}$	$5.5\cdot10^{-8}$	0.79	$3.7\cdot10^{4}$	$7.9\cdot10^{-8}$	0.82	$1.\ 6\cdot10^{7}$	0.002
48 h	$6.2\cdot10^{-8}$	0.84	$1.7\cdot10^{3}$	$5.3\cdot10^{-8}$	0.84	$1.1\cdot10^{4}$	$7.2\cdot10^{-8}$	0.86	$5.1\cdot10^{6}$	0.002
7 d	$6.3\cdot10^{-9}$	1	$2.8\cdot10^{2}$	$6.5\cdot10^{-7}$	0.73	$3.3\cdot10^{4}$	$7.3\cdot10^{-7}$	0.73	$1.8\cdot10^{6}$	0.004
14 d	$2.1\cdot10^{-6}$	0.65	78	$2.7\cdot10^{-6}$	0.94	$6.8\cdot10^{2}$	$2.1\cdot10^{-6}$	0.92	$3.0\cdot10^{5}$	0.01
28 d	$6.3\cdot10^{-9}$	1	$3.3\cdot10^{2}$	$1.3\cdot10^{-6}$	0.73	$4.3\cdot10^{3}$	$1.3\cdot10^{-6}$	0.72	$2.0\cdot10^{6}$	0.003
A-PEO										
1 h	$4.8\cdot10^{-9}$	1	$1.2\cdot10^{3}$	$6.9\cdot10^{-7}$	0.61	$1.2\cdot10^{5}$	$2.6\cdot10^{-7}$	0.95	$1.5\cdot10^{7}$	0.001
48 h	$5.4\cdot10^{-9}$	1	$5.0\cdot10^{2}$	$1.4\cdot10^{-6}$	0.55	$7.8\cdot10^{4}$	$4.8\cdot10^{-7}$	0.96	$5.8\cdot10^{6}$	0.003
7 d	$5.4\cdot10^{-9}$	1	$3.2\cdot10^{2}$	$1.3\cdot10^{-6}$	0.67	$1.8\cdot10^{4}$	$9.8\cdot10^{-7}$	0.92	$1.3\cdot10^{6}$	0.003
14 d	$1.3\cdot10^{-8}$	0.96	$2.2\cdot10^{2}$	$1.3\cdot10^{-6}$	0.85	$5.6\cdot10^{3}$	$1.8\cdot10^{-6}$	0.70	$1.2\cdot10^{6}$	0.005
28 d	$5.2\cdot10^{-9}$	1	$3.2\cdot10^{2}$	$4.3\cdot10^{-6}$	0.67	$2.5\cdot10^{4}$	$7.7\cdot10^{-7}$	1	$7.6\cdot10^{5}$	0.003
A(Cu)-PEO										
1 h	$4.5\cdot10^{-9}$	1	$2.0\cdot10^{3}$	$1.9\cdot10^{-7}$	0.70	$2.0\cdot10^{4}$	$2.3\cdot10^{-7}$	0.79	$4.5\cdot10^{6}$	0.007
48 h	$6.4\cdot10^{-9}$	1	$3.2\cdot10^{2}$	$6.5\cdot10^{-8}$	0.92	$1.0\cdot10^{4}$	$1.6\cdot10^{-7}$	0.80	$1.7\cdot10^{6}$	0.001
7 d	$5.6\cdot10^{-9}$	1	$3.0\cdot10^{2}$	$4.1\cdot10^{-7}$	0.83	$2.8\cdot10^{4}$	$3.9\cdot10^{-8}$	1	$1.3\cdot10^{6}$	0.002
14 d	$4.8\cdot10^{-9}$	1	$5.1\cdot10^{2}$	$1.3\cdot10^{-6}$	0.72	$1.2\cdot10^{4}$	$7.9\cdot10^{-8}$	0.83	$2.1\cdot10^{5}$	0.001
28 d	$1.6\cdot10^{-8}$	0.90	$6.0\cdot10^{2}$	$8.5\cdot10^{-7}$	0.86	$7.4\cdot10^{3}$	$4.7\cdot10^{-7}$	0.90	$9.9\cdot10^{5}$	0.006

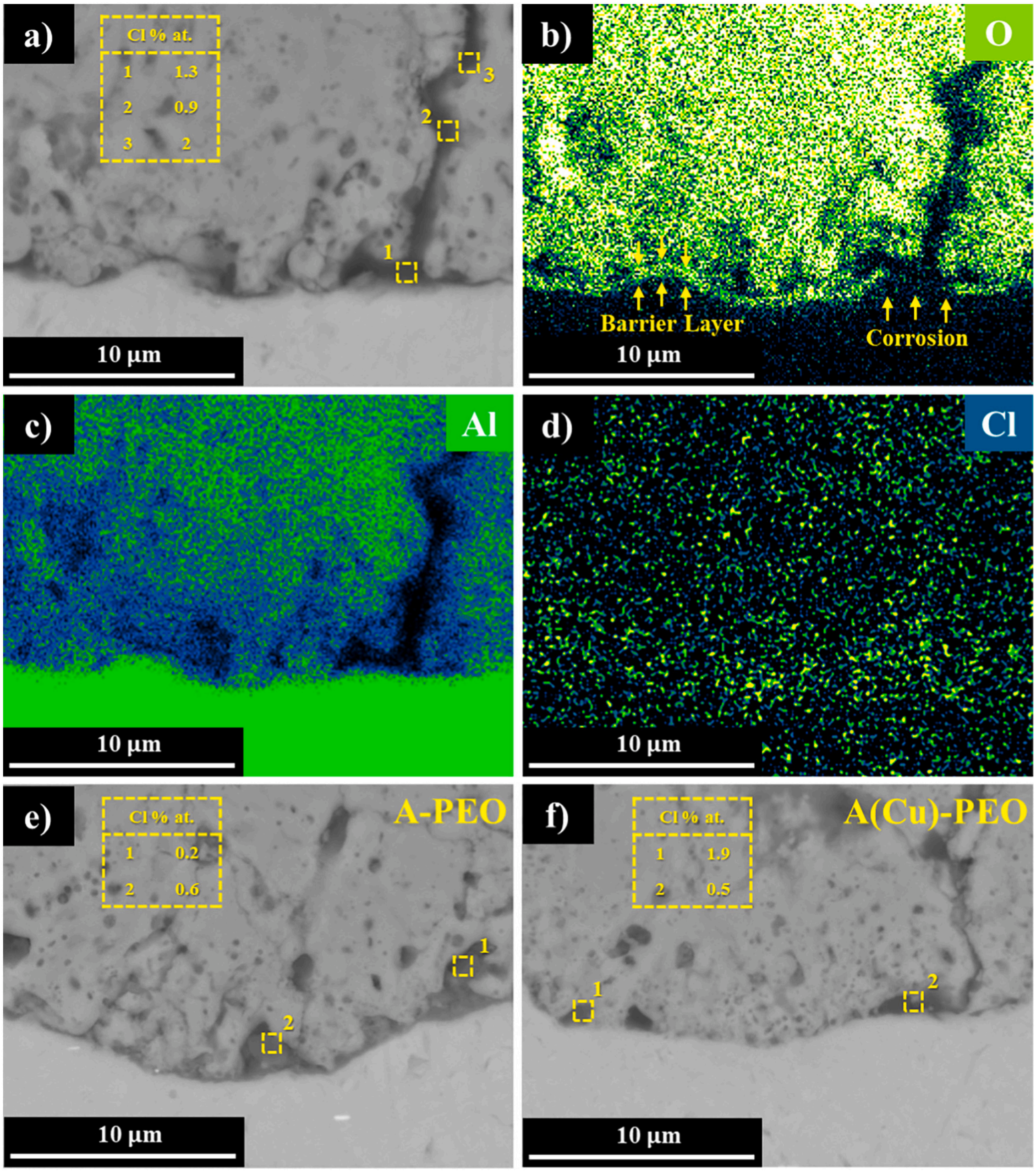

Fig. 22. Cross-sectional SEM images of the PEO (a), A-PEO (e), and A(Cu)-PEO (f) coatings after 28 days of corrosion testing. Oxygen, Aluminium and Chlorine compositional map of the PEO coating (b–d).

4. Conclusions

This work investigated the effect of new anodic film precursor systems with Sn, Cu and Ni electrolytic colouring for PEO treatments on a 1085 Al alloy. The main conclusions can be summarized as follows:

1. An early onset of the soft sparking regime was identified in PEO coatings based on precursor systems. This was accompanied by reduced gas evolution in comparison to direct PEO.
2. The use of 20 µm-thick precursor system enabled an energy saving of ~36 %. Electrolytic colouring of the anodic precursor further improved the energy efficiency. Cu-colouring achieved the highest savings with a ~ 54 % reduction compared to conventional PEO. Sn and Ni provided 51 % and 49 % energy savings, respectively.
3. The A-PEO system showed lower porosity (20.3 %) and a higher α-Al_2O_3/γ-Al_2O_3 ratio (1.35) which was attributed to greater exposure to the soft sparking regime. A low content of Sn, Cu, and Ni (~ 0.1–0.2 at.% for Sn and Ni, and ~ 1.3 at.% for Cu) was detected in the outermost regions of the precursor-based PEO coatings, suggesting that most of these elements were lost into the electrolyte during the PEO treatment.
4. Characterization of the early stages of PEO processing with precursor systems revealed breakdown events at the barrier layer and intermetallics. Coloured precursor systems revealed the onset of microdischarges at the top-end of the deposited metal, appearing as a continuous dark wavemark. This promoted an earlier transition to soft sparking, particularly for the Cu-rich precursor.
5. The system with highest energy efficiency, A(Cu)-PEO, was selected for wear and corrosion testing. Wear tests of PEO and A(Cu)-PEO systems revealed comparable wear rates: (2.3 ± 0.3) · 10^5 and (2.5 ± 0.3) · 10^5 $mm^3 \cdot N^{-1} \cdot m^{-1}$, respectively. The A-PEO system showed lower friction coefficient and wear rate ((2.1 ± 01) · 10^5

$mm^3 \cdot N^{-1} \cdot m^{-1}$) due to its greater compactness and α-Al_2O_3/γ-Al_2O_3 ratio. EIS measurements in 3.5 wt% NaCl revealed progressive degradation of the PEO coatings. The Cu in the precursor compromised the initial level of protection provided by the barrier layer. However, all coatings exhibited negligible substrate damage after 28 days of immersion, indicating that A-PEO and A(Cu)-PEO precursor-based systems are a viable alternative to conventional PEO due to their adequate performance and considerable energy savings.

CRediT authorship contribution statement

I. Hidalgo-González: Writing – review & editing, Writing – original draft, Validation, Methodology, Investigation, Formal analysis, Data curation. **E. Matykina:** Writing – review & editing, Supervision, Project administration, Methodology, Formal analysis, Conceptualization. **R. Arrabal:** Writing – review & editing, Supervision, Project administration, Methodology, Funding acquisition, Formal analysis, Conceptualization.

Declaration of competing interest

The authors declare that they have no known competing financial interests or personal relationships that could have appeared to influence the work reported in this paper.

Acknowledgements

I. Hidalgo-González acknowledges the Universidad Complutense de Madrid and Santander Bank for funding a predoctoral contract (CT 25/24). R. Arrabal acknowledges the funding from Universidad Complutense de Madrid (FEI21/11).

Appendix A. Supplementary data

Supplementary data to this article can be found online at https://doi.org/10.1016/j.surfcoat.2025.133101.

Data availability

All data presented in this work will be made available through Docta Complutense repository. https://docta.ucm.es/handle/20.500.14352/16

References

[1] F.C. Walsh, C.T.J. Low, R.J.K. Wood, K.T. Stevens, J. Archer, A.R. Poeton, Plasma electrolytic oxidation (PEO) for production of anodised coatings on lightweight metal (Al, Mg, Ti) alloys, Trans. Inst. Met. Finish. 87 (2009) 122–135, https://doi.org/10.1179/174591908X372482.

[2] A.L. Yerokhin, X. Nie, A. Leyland, A. Matthews, S.J. Dowey, Plasma electrolysis for surface engineering, Surf. Coat. Technol. 122 (1999) 73–93, https://doi.org/10.1016/S0257-8972(99)00441-7.

[3] B.L. Jiang, Y.M. Wang, Plasma electrolytic oxidation treatment of aluminium and titanium alloys, in: H. Dong (Ed.), Surface Engineering of Light Alloys, Woodhead Publishing, Cambridge, 2010, pp. 110–154, https://doi.org/10.1533/9781845699451.2.110.

[4] R.C. Barik, J.A. Wharton, R.J.K. Wood, K.R. Stokes, R.L. Jones, Corrosion, erosion and erosion-corrosion performance of plasma electrolytic oxidation (PEO) deposited Al_2O_3 coatings, Surf. Coat. Technol. 199 (2005) 158–167, https://doi.org/10.1016/j.surfcoat.2004.09.038.

[5] E. Lopez-Martinez, M. Mohedano, E. Matykina, R. Arrabal, PEO of additively manufactured Al10SiMg alloy: effects of α-Al_2O_3 particles on energy consumption and wear behaviour, J. Mater. Res. Technol. 31 (2024) 1786–1796, https://doi.org/10.1016/j.jmrt.2024.06.171.

[6] X. Lu, M. Mohedano, C. Blawert, E. Matykina, R. Arrabal, K.U. Kainer, Plasma electrolytic oxidation coatings with particle additions - a review, Surf. Coat. Technol. 307 (2016) 1165–1182, https://doi.org/10.1016/j.surfcoat.2016.08.055.

[7] M. Mohedano, X. Lu, E. Matykina, C. Blawert, R. Arrabal, M.L. Zheludkevich, Plasma electrolytic oxidation (PEO) of metals and alloys, in: Encyclopedia of Interfacial Chemistry: Surface Science and Electrochemistry, 2018, pp. 423–438, https://doi.org/10.1016/B978-0-12-409547-2.13398-0.

[8] C.B. Wei, X.B. Tian, S.Q. Yang, X.B. Wang, R.K.Y. Fu, P.K. Chu, Anode current effects in plasma electrolytic oxidation, Surf. Coat. Technol. 201 (2007) 5021–5024, https://doi.org/10.1016/j.surfcoat.2006.07.103.

[9] Zhang X.M, Tian X.B, Yang S.Q, Gong C.Z, Fu R.K, Chu P.K, Low energy-consumption plasma electrolytic oxidation based on grid cathode, Rev. Sci. Instrum. 81 (2010) 103504, https://doi.org/10.1063/1.3500319.

[10] M. Mohedano, E. Lopez, B. Mingo, S. Moon, E. Matykina, R. Arrabal, Energy consumption, wear and corrosion of PEO coatings on preanodized Al alloy: the influence of current and frequency, J. Mater. Res. Technol. 21 (2022) 2061–2075, https://doi.org/10.1016/j.jmrt.2022.10.049.

[11] V. Dehnavi, B.L. Luan, D.W. Shoesmith, X.Y. Liu, S. Rohani, Effect of duty cycle and applied current frequency on plasma electrolytic oxidation (PEO) coating growth behaviour, Surf. Coat. Technol. 226 (2013) 100–107, https://doi.org/10.1016/j.surfcoat.2013.03.041.

[12] L. Ropyak, T. Shihab, A. Velychkovych, V. Bilinskyi, V. Malinin, M. Romaniv, Optimization of plasma electrolytic oxidation technological parameters of deformed aluminium alloy D16T in flowing electrolyte, Ceram 6 (2023) 146–167, https://doi.org/10.3390/ceramics6010010.

[13] C. Blawert, V. Heitmann, W. Dietzel, H.M. Nykyforchyn, M.D. Klapkiv, Influence of electrolyte on corrosion properties of plasma electrolytic conversion coated magnesium alloys, Surf. Coat. Technol. 201 (2007) 8709–8714, https://doi.org/10.1016/j.surfcoat.2006.07.169.

[14] M. Mohedano, B. Mingo, H. Mora-Sánchez, E. Matykina, R. Arrabal, Effects of pre-anodizing and phosphates on energy consumption and corrosion performance of PEO coatings on AA6082, Surf. Coat. Technol. 409 (2021) 126892, https://doi.org/10.1016/j.surfcoat.2021.126892.

[15] M.A. Iqbal, H. Asghar, V. Maurino, E. Matykina, R. Arrabal, M. Mohedano, Evaluating the energy consumption, structural, and corrosion resistance properties of photocatalytic TiO_2-based PEO coatings on pre-anodized AA2024-Al, Surf. Interfaces 44 (2024) 103659, https://doi.org/10.1016/j.surfin.2023.103659.

[16] R. Olmo, M. Mohedano, P. Visser, E. Matykina, R. Arrabal, Flash-PEO coatings loaded with corrosion inhibitors on AA2024, Surf. Coat. Technol. 402 (2020) 126317, https://doi.org/10.1016/j.surfcoat.2020.126317.

[17] R. Olmo, E. López, E. Matykina, U. Tiringer, J.M.C. Mol, M. Mohedano, R. Arrabal, Hybrid PEO/sol-gel coatings loaded with Ce for corrosion protection of AA2024-T3, Prog. Org. Coat. 182 (2023) 107667, https://doi.org/10.1016/j.porgcoat.2023.107667.

[18] Z.U. Rehman, S.H. Shin, I. Hussain, B.H. Koo, Structure and corrosion properties of the two-step PEO coatings formed on AZ91D Mg alloy in K_2ZrF_6-based electrolyte solution, Surf. Coat. Technol. 307 (2016) 484–490, https://doi.org/10.1016/j.surfcoat.2016.09.030.

[19] M.H. Guerra-Mutis, J.M. Vega, E. Matykina, R. Arrabal, Permanganate–fluorozirconate conversion coating as precursor for Flash-PEO on AZ31B magnesium alloy, Ceram. Int. (2025) 10.101, https://doi.org/10.1016/j.ceramint.2025.10.101.

[20] A.L. Yerokhin, A. Shatrov, V. Samsonov, P. Shashkov, A. Pilkington, A. Leyland, et al., Oxide ceramic coatings on aluminium alloys produced by a pulsed bipolar plasma electrolytic oxidation process, Surf. Coat. Technol. 199 (2005) 150–157, https://doi.org/10.1016/j.surfcoat.2004.10.147.

[21] X. Xie, E. Yang, Z. Zhang, W. Wei, D. Li, X. Zhao, R. Yang, W. Li, Effects of K_2TiF_6 and electrolyte temperatures on energy consumption and properties of MAO coatings on 6063 aluminum alloy, Materials 16 (2023) 1830, https://doi.org/10.3390/ma16051830.

[22] H. Tian, Y. Zhang, X. Hao, H. Zhang, W. Wu, G. Han, Z. Dou, Y. Wei, Y. Zhang, F. Chen, Preparation and characterization of the low-energy plasma electrolysis oxide coatings on Mg–Li alloy, Surf. Coat. Technol. 440 (2022) 128445, https://doi.org/10.1016/j.surfcoat.2022.128445.

[23] K. Li, G. Zhang, A. Yi, W. Zhu, Z. Liao, K. Chen, et al., Effects of matrix silicon content on the plasma electrolytic oxidation of Al–Si alloys using different power modes, Crystals 12 (2022) 123, https://doi.org/10.3390/cryst12010123.

[24] M.A. Iqbal, E. Matykina, R. Arrabal, M. Mohedano, Role of anodic precursor layer thickness on PEO coatings: energy consumption and long-term corrosion performance, Surf. Coat. Technol. 476 (2024) 130186, https://doi.org/10.1016/j.surfcoat.2023.130186.

[25] E. Matykina, R. Arrabal, P. Skeldon, G.E. Thompson, P. Belenguer, AC PEO of aluminium with porous alumina precursor films, Surf. Coat. Technol. 205 (2010) 1668–1678, https://doi.org/10.1016/j.surfcoat.2010.05.014.

[26] A.B. Rogov, A. Yerokhin, A. Matthews, The role of cathodic current in plasma electrolytic oxidation of aluminium: phenomenological concepts of the “soft sparking” mode, Langmuir 33 (2017) 11059–11069, https://doi.org/10.1021/acs.langmuir.7b02284.

[27] W. Geebarowski, S. Pietrzyk, Influence of the cathodic pulse on the formation and morphology of oxide coatings on aluminium produced by plasma electrolytic oxidation, Arch. Metall. Mater. 58 (2013) 241–245, https://doi.org/10.2478/v10172-012-0180-7.

[28] J. Martin, A.V. Nominé, J. Stef, A. Nominé, J.X. Zou, G. Henrion, T. Grosdidier, The influence of metallurgical state of substrate on the efficiency of plasma electrolytic oxidation (PEO) process on magnesium alloy, Mater. Des. 178 (2019) 107859, https://doi.org/10.1016/j.matdes.2019.107859.

[29] H. Mora-Sanchez, R. del Olmo, J. Rams, B. Torres, M. Mohedano, E. Matykina, R. Arrabal, Hard anodizing and plasma electrolytic oxidation of an additively manufactured Al–Si alloy, Surf. Coat. Technol. 420 (2021) 127339, https://doi.org/10.1016/j.surfcoat.2021.127339.

[30] B.L. Pereira, T. Gontarski, L.C. Fontana, C.M. Lepienski, A. Bhattacharjee, K. Popat, R.D. Torres, P. Soares, Surface modification of stainless steel via TMS and PEO for

biomedical applications, Surf. Coat. Technol. 513 (2025) 132533, https://doi.org/10.1016/j.surfcoat.2025.132533.

[31] E. Matykina, R. Arrabal, P. Skeldon, G.E. Thompson, Mechanism of PEO coating growth on titanium, in: T. Sudarshan, M. Jeandin (Eds.), Surface Modification Technologies, Proc. 21st Int. Conf. Surface Modification Technologies (SMT-21), Paris, 2007, VALAR Docs, 2008, pp. 339–347.

[32] S. Fajardo, G.S. Frankel, Gravimetric method for hydrogen evolution measurements on dissolving magnesium, J. Electrochem. Soc. 162 (2015) C693–C701, https://doi.org/10.1149/2.0241514jes.

[33] W. Lee, S.J. Park, Porous anodic aluminium oxide: anodization and templated synthesis of functional nanostructures, Chem. Rev. 114 (2014) 7487–7556, https://doi.org/10.1021/cr500002z.

[34] A.S. Doughty, G.E. Thompson, J.A. Richardson, G.C. Wood, Investigation of the electrolytic colouring of porous anodic films on aluminium using electron microscopy, Trans. Inst. Met. Finish. 53 (1975) 33–39, https://doi.org/10.1080/00202967.1975.11870335.

[35] K. Liang, C.H. Liang, H. Wang, Structure and distribution of electrodeposits on anodic aluminium films by electrolytic colouring in zinc sulphate solution, Trans. Inst. Met. Finish. 85 (2007) 159–161, https://doi.org/10.1179/174591907X192267.

[36] G. Zangari, Fundamentals of electrodeposition, in: Encyclopedia of Interfacial Chemistry: Surface Science and Electrochemistry, 2018, pp. 141–160, https://doi.org/10.1016/B978-0-12-409547-2.11700-7.

[37] P. Afsin, C. Akyil, K. Kazmanli, M. Ürgen, Electro-colouring mechanism of aluminium anodic oxides in tin-based electrolytes, Coatings 14 (2024) 616, https://doi.org/10.3390/coatings14050616.

[38] F.C. Walsh, C.T.J. Low, A review of developments in the electrodeposition of tin, Surf. Coat. Technol. 288 (2016) 79–94, https://doi.org/10.1016/j.surfcoat.2015.12.081.

[39] T.W. Clyne, S.C. Troughton, A review of recent work on discharge characteristics during plasma electrolytic oxidation of various metals, Int. Mater. Rev. 64 (2019) 127–162, https://doi.org/10.1080/09506608.2018.1466492.

[40] V.A. Golovenko, O.A. Kalinichenko, E.V. Roenko, N.L. Gurevina, L.A. Snezhko, Analysis of gaseous products of plasma electrolytic oxidation of aluminium, Surf. Eng. Appl. Electrochem. 55 (2019) 191–196, https://doi.org/10.3103/S1068375519020108.

[41] K. Wei, Y. Zhang, J. Yu, R. Liu, J. Du, F. Jiang, Analyses of hydrogen release on zirlo alloy anode during plasma electrolytic oxidation, Mater. Chem. Phys. 251 (2020) 123054, https://doi.org/10.1016/j.matchemphys.2020.123054.

[42] Y. Cheng, Z. Peng, X. Wu, J. Cao, P. Skeldon, G.E. Thompson, A comparison of plasma electrolytic oxidation of Ti-6Al-4V and Zircaloy-2 alloys in a silicate-hexametaphosphate electrolyte, Electrochim. Acta 165 (2015) 301–313, https://doi.org/10.1016/j.electacta.2015.03.020.

[43] L.O. Snizhko, A.L. Yerokhin, A. Pilkington, N.L. Gurevina, D.O. Misnyankin, A. Leyland, Anodic processes in plasma electrolytic oxidation of aluminium in alkaline solutions, Electrochim. Acta 49 (2004) 2085–2095, https://doi.org/10.1016/j.electacta.2003.11.027.

[44] A.B. Rogov, A. Nemcova, T. Hashimoto, A. Matthews, A. Yerokhin, Analysis of electrical response, gas evolution and coating morphology during transition to soft sparking PEO of Al, Surf. Coat. Technol. 442 (2022) 128142, https://doi.org/10.1016/j.surfcoat.2022.128142.

[45] E. Matykina, R. Arrabal, A. Pardo, M. Mohedano, B. Mingo, I. Rodríguez, Energy-efficient PEO process of aluminium alloys, Mater. Lett. 127 (2014) 13–16, https://doi.org/10.1016/j.matlet.2014.04.077.

[46] H.H. Shih, Y.C. Huang, Study on the black electrolytic colouring of anodized aluminium in cupric sulfate, J. Mater. Process. Technol. 208 (2008) 24–28, https://doi.org/10.1016/j.jmatprotec.2007.12.119.

[47] E. Matykina, R. Arrabal, P. Skeldon, G.E. Thompson, Investigation of the growth processes of coatings formed by AC plasma electrolytic oxidation of aluminium, Electrochim. Acta 54 (2009) 6767–6778, https://doi.org/10.1016/j.electacta.2009.06.088.

[48] E. Matykina, G. Doucet, F. Monfort, A. Berkani, P. Skeldon, G.E. Thompson, Destruction of coating material during spark anodizing of titanium, Electrochim. Acta 51 (2006) 4709–4715, https://doi.org/10.1016/j.electacta.2006.01.021.

[49] J. Martin, A. Nominé, V. Ntomprougkidis, S. Migot, S. Bruyère, F. Soldera, Formation of a metastable nanostructured mullite during plasma electrolytic oxidation of aluminium in 'soft' regime condition, Mater. Des. 180 (2019) 107977, https://doi.org/10.1016/j.matdes.2019.107977.

[50] J.A. Curran, T.W. Clyne, Thermo-physical properties of plasma electrolytic oxide coatings on aluminium, Surf. Coat. Technol. 199 (2005) 168–176, https://doi.org/10.1016/j.surfcoat.2004.09.037.

[51] E. Bousser, A. Rogov, P. Shashkov, A. Gholinia, N. Laugel, T.J.A. Slater, Phase transitions in alumina films during post-sparking anodising of Al alloys, Acta Mater. 244 (2023) 118587, https://doi.org/10.1016/j.actamat.2022.118587.

[52] F. Jaspard-Mécuson, T. Czerwiec, G. Henrion, T. Belmonte, L. Dujardin, A. Viola, Tailored aluminium oxide layers by bipolar current adjustment in the plasma electrolytic oxidation (PEO) process, Surf. Coat. Technol. 201 (2007) 8677–8682, https://doi.org/10.1016/j.surfcoat.2006.09.005.

[53] K. Okada, A. Hattori, T. Taniguchi, A. Nukui, R. Nath Das, Effect of divalent cation additives on the γ- Al_2O_3 to α- Al_2O_3 phase transition, J. Am. Ceram. Soc. 83 (2000) 928–932, https://doi.org/10.1111/j.1151-2916.2000.tb01296.x.

[54] R. Arrabal, M. Mohedano, E. Matykina, A. Pardo, B. Mingo, M.C. Merino, Characterization and wear behaviour of PEO coatings on 6082-T6 aluminium alloy with incorporated α-Al_2O_3 particles, Surf. Coat. Technol. 269 (2015) 64–73, https://doi.org/10.1016/j.surfcoat.2014.10.048.

[55] A.L. Yerokhin, L.O. Snizhko, N.L. Gurevina, A. Leyland, A. Pilkington, A. Matthews, Discharge characterization in plasma electrolytic oxidation of aluminium, J. Phys. D: Appl. Phys. 36 (2003) 2110–2120, https://doi.org/10.1088/0022-3727/36/17/314.

[56] E. Matykina, R. Arrabal, M. Mohedano, B. Mingo, J. Gonzalez, A. Pardo, Recent advances in energy efficient PEO processing of aluminium alloys, Trans. Nonferrous Metals Soc. China 27 (2017) 1439–1454, https://doi.org/10.1016/S1003-6326(17)60166-3.

[57] Y.J. Oh, J.I. Mun, J.H. Kim, Effects of alloying elements on microstructure and protective properties of Al_2O_3 coatings formed on aluminium alloy substrates by plasma electrolysis, Surf. Coat. Technol. 204 (2009) 141–148, https://doi.org/10.1016/j.surfcoat.2009.07.002.

[58] H. Habazaki, X. Zhou, P. Skeldon, G.E. Thompson, G.C. Wood, Mobility of copper ions in anodic alumina films, Electrochim. Acta 42 (1997) 2627–2635, https://doi.org/10.1016/S0013-4686(96)00454-9.